

# 1 Processing Multiple GNSS RO Data Using FSI and ROPP: Results from the ROMEX

2  
3 Yong Chen<sup>1</sup>, Xinjia Zhou<sup>2</sup>, Xin Jing<sup>3</sup>, Shu-Peng Ho<sup>1</sup>, Xi Shao<sup>3</sup>, and Tung-Chang Liu<sup>3</sup>

4 <sup>1</sup>NOAA/NESDIS/STAR, College Park, MD, 20740, USA

5 <sup>2</sup>ERT, Laurel, MD, 20707, USA

6 <sup>3</sup>CISESS/ESSIC, University of Maryland, College Park, MD, 20740, USA

7 Corresponding to: Yong Chen ([Yong.Chen@noaa.gov](mailto:Yong.Chen@noaa.gov))

## 8 9 Abstract

10  
11 Global Navigation Satellite System (GNSS) Radio Occultation (RO) is a vital technique in  
12 atmospheric remote sensing, providing all-weather, high-resolution vertical observations that  
13 support numerical weather prediction (NWP) and atmospheric research. To enhance  
14 understanding of GNSS RO processing uncertainties and inter-algorithm consistency,  
15 NOAA/STAR developed an independent RO inversion algorithm based on the Full Spectrum  
16 Inversion (FSI) technique to derive bending angle and refractivity profiles from excess phase  
17 data. As part of the international Radio Occultation Modeling Experiment (ROMEX), endorsed  
18 by the International Radio Occultation Working Group (IROWG), STAR's FSI results were  
19 systematically compared with outputs from the community standard Radio Occultation  
20 Processing Package (ROPP) and EUMETSAT datasets. Leveraging multi-GNSS RO  
21 observations from both commercial and government-funded missions, the study evaluates  
22 consistency across processing approaches using the European Centre for Medium-Range  
23 Weather Forecasts (ECMWF) Reanalysis v5 (ERA5) as the reference and structural differences  
24 against the three-dataset mean for the ROMEX period. Results reveal high overall agreement,  
25 while identifying variations linked to the signal-to-noise ratio (SNR) and mission  
26 characteristics, providing critical insights for interpreting ROMEX forecast impact studies and  
27 improving GNSS RO data assimilation systems.

## 28 29 1. Introduction

30  
31 Global Navigation Satellite System (GNSS) Radio Occultation (RO) has become a cornerstone  
32 of atmospheric remote sensing, offering high vertical resolution, global coverage, long-term  
33 stability, and minimal bias (Kursinski et al., 1997; Anthes et al., 2008; Ho et al., 2020). By  
34 measuring the bending of GNSS signals as they pass through the atmosphere, RO enables  
35 retrievals of refractivity, temperature, pressure, and humidity profiles. As a limb-sounding  
36 technique, it is largely unaffected by clouds and precipitation, providing an all-weather  
37 observing capability essential for weather forecasting and climate monitoring (Cucurull et al.,  
38 2007; Healy, 2008; Steiner et al., 2020).

39  
40 Over the past two decades, the expansion of GNSS constellations (e.g., GPS, GLONASS,  
41 Galileo, BeiDou) and the increasing availability of RO missions, including government-funded  
42 programs (e.g., COSMIC-1/2, Metop-A/B/C, Sentinel-6) and commercial ventures (e.g., Spire,  
43 GeoOptics, PlanetiQ), have significantly increased the volume of RO observations (Anthes,  
44 2011; Schreiner et al., 2020; Ho et al., 2023). Today, global RO data counts exceed 35,000-  
45 40,000 profiles per day, with substantial contributions from commercial providers through  
46 initiatives such as NOAA's Commercial Data Purchase (CDP) program. While this growth  
47 enhances the value of RO for numerical weather prediction (NWP) and climate applications, it  
48 also introduces challenges due to differences in instrument design, tracking strategies,  
49 sampling patterns, and processing methodologies.

51 RO retrievals involve several steps: i) deriving clock-synchronized excess phase and signal-to-  
52 noise ratio (SNR) data, ii) inverting excess phase to bending angle (BA) profiles, and iii)  
53 retrieving refractivity from BA via Abel or statistical methods (Gorbunov, 2002a). In the lower  
54 troposphere, strong gradients and multipath propagation complicate retrievals, motivating  
55 advanced inversion techniques such as Full Spectrum Inversion (FSI) (Jensen et al., 2003;  
56 Adhikari et al., 2016, 2021), Canonical Transform Type 2 (CT2) (Gorbunov et al., 2005), and  
57 Phase Matching (PM) (Jensen et al., 2004; Sokolovskiy et al., 2011). FSI relies on explicit  
58 signal localization to enhance vertical resolution and mitigate multipath by reducing spectral  
59 mixing, whereas CT2 achieves an implicit, physics-based localization in impact parameter  
60 space, enabling more robust separation of multipath contributions. As a result, FSI is generally  
61 more sensitive to fine-scale atmospheric structures but also more noise-sensitive, while CT2  
62 provides more stable retrievals in strong multipath conditions at the expense of reduced small-  
63 scale resolution. Among these, FSI has demonstrated particular strength in resolving fine-scale  
64 atmospheric structures.

65  
66 The international RO community is currently undertaking a coordinated effort to evaluate the  
67 impact of large volumes of RO data on NWP. This initiative, known as the Radio Occultation  
68 Modeling Experiment (ROMEX), is endorsed by the International Radio Occultation Working  
69 Group (IROWG) (<https://irowg.org/ro-modeling-experiment-romex/>) and provides a  
70 collaborative platform for data providers and processing centers to assess RO retrievals under  
71 a standardized framework (Anthes et al., 2024). GNSS RO observations from a broad range of  
72 government-funded and commercial missions were submitted to EUMETSAT for centralized  
73 processing, and the resulting products were distributed via the Radio Occultation Meteorology  
74 Satellite Application Facility (ROM SAF). ROMEX provides a standardized framework for  
75 assessing inter-mission and inter-algorithm differences. Central questions include whether  
76 assimilating larger RO volumes improves forecasts, and how variations in data quality and  
77 inversion methods affect the outcome.

78  
79 In support of ROMEX, the NOAA Center for Satellite Applications and Research (STAR)  
80 contributed independent datasets processed using the FSI algorithm (RFSI), which was  
81 integrated into version 10.0 of the Radio Occultation Processing Package (ROPP) (ROPP,  
82 2020). This customized system, hereafter referred to as STAR ROPP, retains compliance with  
83 ROPP standards while incorporating STAR-developed retrieval with the capability, including  
84 both to select the CT2 and FSI methods for bending angle retrieval, ensures compliance with  
85 ROPP standards while incorporating STAR-developed retrieval methods. Here, STAR RFSI  
86 denotes the STAR implementation of the FSI-based bending angle retrieval, while STAR  
87 ROPP refers to the customized ROPP v10.0 framework developed at STAR that supports both  
88 CT2 and FSI processing. This system is distinct Distinguishing STAR ROPP from the official  
89 ROM SAF ROPP, which serves as the community standard. In this study, the community-  
90 standard dataset refers specifically to data generated using the STAR ROPP CT2 method.  
91 Maintaining this distinction processing is critical essential, as it enables an independent  
92 assessment of algorithmic effects on RO data quality.

93  
94 FSI is theoretically well suited for resolving fine-scale atmospheric structures and handling  
95 multipath in the lower troposphere (Jensen et al., 2003; Adhikari et al., 2021), a key source of  
96 uncertainty for NWP. The use of the STAR RFSI algorithm within ROMEX is therefore to  
97 quantify the structural uncertainty associated with this alternative, high-resolution retrieval  
98 approach relative to community-standard methods, thereby providing critical insight for  
99 optimizing multi-mission data assimilation strategies.

100

101 This study evaluates the STAR FSI-based processing system (~~RFSI~~) within the ROMEX  
102 framework. Retrievals from RFSI are compared against those from the STAR ROPP with the  
103 CT2 method and the EUMETSAT-processed ROMEX dataset (with COSMIC-2 data provided  
104 by UCAR). The analysis focuses on November 2022 and utilizes the European Centre for  
105 Medium-Range Weather Forecasts (ECMWF) Reanalysis v5 (ERA5) (Hersbach et al., 2023)  
106 as a reference to evaluate algorithmic performance across various missions. The STAR RFSI  
107 dataset for ROEMEX is one of the three RO datasets, along with those from EUMETSAT and  
108 UCAR, that were released to ROMEX participants through ROM-SAF (Shao and Folsche,  
109 2024).

110  
111 Intercomparisons included statistical evaluations (mean biases, standard deviations) and inter-  
112 algorithm consistency. This design helps isolate processing-related uncertainties (e.g.,  
113 structural uncertainty; Ho et al., 2012) and ensures that differences in NWP impact can be  
114 attributed to data quality and processing methodology rather than uncontrolled input or  
115 evaluation effects.

116  
117 The paper is organized as follows: Session 2 describes the GNSS RO observations and datasets  
118 used in this study. Session 3 presents the FSI algorithm in detail. Session 4 provides inter-  
119 algorithm and inter-mission comparison results using ROMEX RO data. Conclusions are  
120 summarized in session 5.

121

## 122 **2. GNSS RO Observations and Data Used in this Study**

### 123 **2.1 GNSS RO Observations**

124  
125 Modern satellite missions, including COSMIC-2, Spire, and PlanetiQ, have significantly  
126 increased the volume of GNSS radio occultation data. These missions track signals from  
127 multiple constellations, including GPS, GLONASS, Galileo, and BeiDou, thereby improving  
128 global spatial and temporal coverage for atmospheric profiling.

129  
130 LEO satellite receivers track GNSS signals using two primary methods: Closed Loop (CL) and  
131 Open Loop (OL). CL tracking ensures stable signal acquisition in the upper atmosphere but  
132 may fail under rapidly varying conditions in the lower troposphere. OL tracking, by contrast,  
133 is specifically designed to capture multipath-affected signals in the lower atmosphere. ~~The~~  
134 combination use of CL and OL tracking was traditionally adopted to ensure enables robust  
135 reliable performance across the full vertical extent of the atmosphere. However, recent GNSS  
136 radio occultation missions, including COSMIC-2, Spire, and PlanetiQ, primarily employ OL  
137 tracking throughout the occultation in order to maximize tracking robustness and data  
138 continuity across all atmospheric layers.

139  
140 The raw data, consisting of signal phase and amplitude measurements, are processed to  
141 calculate bending angle and refractivity profiles. A critical step in this process is correcting  
142 ionospheric effects. This is achieved by using dual-frequency signals (e.g., L1 and L2), which  
143 allow separation of the frequency-dependent ionospheric interference from the non-dispersive  
144 signal of the neutral atmosphere. This isolation is essential for accurate atmospheric retrievals.

145

### 146 **2.2 RO Data Used in this Study**

147  
148 This study utilizes Level 1b atmospheric excess phase data (in conPhs/atmPhs format) from  
149 the ROMEX campaign. The dataset includes contributions from commercial providers, such  
150 as PlanetiQ, Spire, and GeoOptics, as well as government-funded missions, including Metop-

151 B/C and COSMIC-2. A summary of mission-specific data coverage for the period 1 September  
 152 to 30 November 2022 is provided in Table 1. These excess phase datasets, delivered in NetCDF  
 153 format and available exclusively to ROMEX participants, serve as the primary input for  
 154 deriving neutral atmospheric bending angle and refractivity profiles. On average, the dataset  
 155 comprises approximately 37,790 profiles per day.

156  
 157 The high scientific value and cost-effectiveness of GNSS RO technology have driven increased  
 158 private-sector participation in recent years. U.S. companies Spire Global, PlanetiQ, and  
 159 GeoOptics, along with Yunyao Aerospace in China, have deployed RO receivers on  
 160 commercial satellites to supply high-quality data to the scientific community. Among them,  
 161 Spire Global Inc. contributes approximately 17,000 profiles per day to ROMEX, followed by  
 162 Yunyao Aerospace with about 6,200, PlanetiQ with about 3,300, and GeoOptics with roughly  
 163 300.

164  
 165 Several government-funded RO satellite missions were routinely processed by the UCAR  
 166 COSMIC Data Analysis and Archive Center (CDAAC) and made available to both the research  
 167 and operational communities during the ROMEX period. These missions include COSMIC-2  
 168 (~6,000 profiles/day), KOMPSAT-5 (~300), PAZ (~200), and both TerraSAR-X and  
 169 TanDEM-X (~100 each). RO data from Metop-B/C and Sentinel-6 were provided by  
 170 EUMETSAT, delivering approximately 1,200 and 800 profiles per day, respectively. RO  
 171 profiles from FY-3C/D/E and Tianmu were supplied by the National Satellite Meteorological  
 172 Center (NSMC) of the Chinese Meteorological Administration (CMA) and the National Space  
 173 Science Center (NSSC) of the Chinese Academy of Sciences (CAS), respectively, with average  
 174 daily counts of approximately 2,100 and 1300.

175  
 176 For this study, we processed RO data from all ROMEX missions except Sentinel-6 and  
 177 GeoOptics, as well as from the Chinese government or Chinese companies (e.g., FY-3,  
 178 Yunyao, and Tianmu). For each processed mission, we generated bending angle and  
 179 refractivity profiles using both the STAR RFSI and STAR ROPP (CT2) algorithms. These  
 180 datasets were submitted to EUMETSAT and distributed to ROMEX participants through the  
 181 ROM SAF. By processing multiple missions with independent algorithms, we ensured  
 182 consistent inputs across platforms. We enabled a direct assessment of algorithm-dependent  
 183 uncertainties, thereby clarifying how data processing influences the interpretation of ROMEX  
 184 NWP impact experiments. [Table 2 summarizes the typical SNR characteristics of GNSS](#)  
 185 [receivers across different missions, supporting the discussion of mission-dependent](#)  
 186 [performance and structural uncertainties.](#)

187  
 188 Table 1: RO Missions are included in ROMEX

RO mission	RO profiles/day	Excess phase provider	STAR ROPP/RFSI	EUMETSAT
Metop B, C (GRAS)	1200	EUMETSAT	√	√
COSMIC-2	6000	UCAR	√	√ <sup>#</sup>
SPIRE	17000	Spire	√	√ <sup>*</sup>
PlanetiQ	3300	PlanetiQ	√	√ <sup>*</sup>
GeoOptics	300	GeoOptics	x	√
KOMPSAT-5	300	UCAR	√	√
PAZ	200	UCAR	√	√
TerraSAR-X	100	UCAR	√	√

TanDEM-X	100	UCAR	√	√
Sentinel-6	800	EUMETSAT	x	√
FY3-C, D, E (GNOS)	2100	CMA/NSMC	x	√
Yun Yao	6200	Yun Yao	x	√
Tianmu	<del>1300</del>	CAS/NSSC	x	√
ROMEX total	<del>377900</del>			

√<sup>#</sup> UCAR provided both bending angle and refractivity in the EUMETSAT ROMEX dataset.  
 √\* No refractivity available in the EUMETSAT dataset for PlanetiQ and Spire, only bending angle

Table 2 Signal-to-Noise Ratio (SNR)<sup>#</sup> characteristics of GNSS receivers across different missions

<u>RO mission</u>	<u>GPS</u>	<u>GLONASS</u>	<u>Galileo</u>	<u>BeiDou</u>
<u>Metop B</u>	<u>730.2</u>	-	-	-
<u>Metop C</u>	<u>789.3</u>	-	-	-
<u>COSMIC-2</u>	<u>1295.1</u>	<u>1181.4</u>	-	-
<u>SPIRE</u>	<u>387.9</u>	<u>707.2</u>	<u>316.4</u>	-
<u>PlanetiQ</u>	<u>1440.5</u>	<u>1580.6</u>	<u>1124.8</u>	<u>1335.7</u>
<u>KOMPSAT-5</u>	<u>617.2</u>	-	-	-
<u>PAZ</u>	<u>503.9</u>	-	-	-
<u>TerraSAR-X</u>	<u>622.4</u>	-	-	-
<u>TanDEM-X</u>	<u>549.3</u>	-	-	-

<sup>#</sup> Mean SNR between altitudes 60 km and 80 km, with unit (volt/volt)

### 3. Full Spectrum Inversion Algorithm and Processing Chain

The core FSI algorithm remains consistent with that described in Adhikari et al. (2021). The novelty of the present work lies in the development and presentation of the complete STAR RFSI end-to-end processing framework (including data preprocessing, quality control, and statistical optimization) and its systematic, harmonized application to the large and diverse multi-mission ROMEX dataset for comprehensive assessment of structural uncertainties against other major processing centers (such as EUMETSAT and UCAR). The STAR RFSI algorithm provides a robust framework for generating bending-angle and refractivity profiles from GNSS RO measurements, particularly in the presence of lower-tropospheric multipath. As described by Chen et al. (2024), the STAR RFSI algorithm has been integrated into ROPP version 10.0 (ROPP, 2020) customized at NOAA STAR. RFSI processes dual-frequency excess phase and SNR data along with satellite position and timing information. It supports a wide range of satellite missions and tracking configurations.

The STAR RFSI end-to-end process involves four main steps (see Fig. 1):

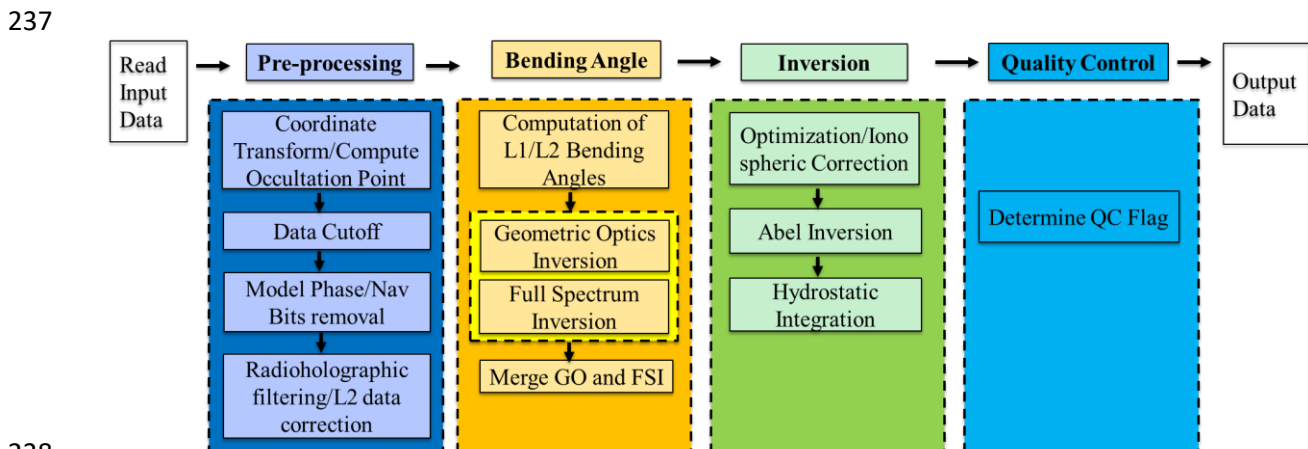
(1) data input and pre-processing: RO data, including satellite geometry, excess phase, and SNR measurements, are ingested and prepared for further processing. Satellite coordinates, if provided at lower frequencies, are interpolated to align with the sampling time using clock bias-corrected transmitter and receiver times (see Section 3.1).

220 (2) bending angle calculation: excess phase data are converted to bending angles, with  
 221 ionospheric corrections applied using dual-frequency measurements (see Section 3.2).

222  
 223 (3) inversion to refractivity and dry temperature: bending angles are inverted using Abel  
 224 integration to derive refractivity profiles, which can subsequently be used to compute dry  
 225 atmospheric temperature (see Section 3.3).

226  
 227 (4) quality control (QC): a comprehensive quality assessment is conducted by applying quality  
 228 flags based on threshold criteria for bending angle differences, determined through  
 229 comparisons with ERA5 simulations. This process ensures that only high-quality profiles are  
 230 retained as valid (see Section 3.4). Additionally, we have developed an internal quality control  
 231 system designed explicitly for near-real-time processing. This internal check was not included  
 232 in the ROMEX data when it was generated.

233  
 234 Figure 1 illustrates the complete RO data processing workflow implemented in the STAR FSI  
 235 system, highlighting the transition from raw signal acquisition to the generation of quality-  
 236 controlled atmospheric profiles (bending angle and refractivity).



238  
 239  
 240 Fig. 1: Flow chart depicting the steps used in the FSI RO data processing of the geometry and  
 241 phase data.

### 242 243 3.1 Data Input and Pre-processing

244  
 245 The STAR RFSI system ingests Level 1b dual-frequency excess phase and SNR data, along  
 246 with satellite position and time information, to generate high-resolution atmospheric profiles.  
 247 The geometry files typically contain satellite position vectors at a lower sampling rate (e.g., 1  
 248 Hz), whereas the excess phase and SNR are sampled at higher rates (e.g., 50-100 Hz). To align  
 249 these data, satellite coordinates are interpolated to the excess-phase sampling times using  
 250 clock-bias-corrected receiver and transmitter times. Satellite geometry and excess phase/SNR  
 251 time series are interpolated into a common sampling rate. Given start time ( $t_s$ ), sampling time  
 252 ( $t$ ), and clock bias-corrected receiver time ( $t_{orb}$ ) and transmitter time ( $t_{txm}$ ), the interpolated  
 253 receiver coordinates ( $r_{leo}$ ), transmitter time ( $t_{txmHR}$ ), and GNSS coordinates ( $r_{gns}$ ) can be  
 254 calculated using cubic spline simple quadratic interpolation as:

255  
 256 
$$r_{leo} = interpolate(r_{leoLR}, t_{orb}, t + t_s, /cubic\_splinequadratic) \quad (1)$$

257  
 258 
$$t_{txmHR} = interpolate(t_{txm}, t_{orb}, t + t_s) \quad (2)$$

259  
 260  $r_{gns} = interpolate(r_{gnsLR}, t_{txm}, t_{txmHR}, /cubic\_splinequadratic)$  (3)  
 261

262 where  $r_{leoLR}$  and  $r_{gnsLR}$  are the original coordinates.  
 263

264 The time series of satellite positions is initially provided in the Earth-Centered Inertial (ECI)  
 265 J2000 frame. These positions are converted to Earth-Centered Earth-Fixed (ECEF) coordinates  
 266 according to the IERS 2010 conventions, which include corrections for polar motion and Earth  
 267 rotation (Adhikari et al., 2021; Petit and Luzum, 2010; Luzum and Petit, 2010). This  
 268 transformation enables geolocation of the occultation tangent point at each time step.  
 269

270 To satisfy the assumption of local spherical symmetry during inversion, occultation geometry  
 271 is reprojected to the local center of curvature. ~~The intersection of the line of sight with the~~  
 272 ~~WGS84 ellipsoid defines t~~The tangent point location on the reference ellipsoid (WGS84) is  
 273 determined where the straight line between the transmitter and receiver touches the ellipsoid.  
 274 The latitude, longitude, ~~and~~ local radius of curvature, and the center of curvature are computed  
 275 at this reference tangent point and used to shift both GNSS and LEO positions into a local  
 276 spherical coordinate system. This step ensures accurate mapping of impact parameters and  
 277 tangent altitudes for each ray path.  
 278

279 RO signals acquired using OL tracking may contain low-SNR regions near the surface due to  
 280 signal fading or tracking loss (see Figure 5 in Adhikari et al., 2021). An appropriate cut-off  
 281 height is essential to ensure the accuracy and reliability of tropospheric information retrieved  
 282 from GNSS signals in OL tracking mode (Sokolovskiy et al., 2009; Sokolovskiy et al., 2010;  
 283 Adhikari et al., 2021; Paoletta et al., 2025). To prevent the propagation of noise-contaminated  
 284 signals through the inversion chain, a systematic signal truncation method is employed using  
 285 SNR-based thresholds in this study. The truncation procedure includes the following steps: (1)  
 286 initial cut-off impact height: the initial threshold of impact height is set based on the LEO  
 287 satellite's altitude, as it influences the signal's penetration depth and the quality of retrieved  
 288 atmospheric profiles; (2) dynamic background SNR calculation: the background SNR is  
 289 estimated for each time series using the lowest 10 seconds of the smoothed data. A 3-second  
 290 moving average is applied to the time series to smooth out high-frequency fluctuations; (3)  
 291 initial SNR threshold determination: starting from the lowest point in the time series, the first  
 292 point where the SNR exceeds three times the calculated background SNR in step (2) is  
 293 identified as a preliminary threshold. (4) final cut-off point selection: moving backward from  
 294 the uppermost point identified in step (3), the cut-off point is determined as the first point where  
 295 the SNR drops below 1.5 times the background SNR, and the associated impact height is higher  
 296 than the threshold established in step (1).  
 297

298 This filtering removes anomalous low-level SNR spikes, which can occur due to OL tracking  
 299 artifacts, particularly in tropical and high-humidity conditions. Improper truncation can  
 300 degrade the quality of bending angle measurements: truncating too high removes real signals,  
 301 introducing a negative bias, while truncating too low retains noise, leading to oscillations in  
 302 the retrieved profiles. The chosen thresholds aim to maximize vertical coverage without  
 303 sacrificing data quality.  
 304

### 305 **3.2 Computation of Bending Angles using Full Spectrum Inversion**

306

307 Bending angle retrieval is performed in two steps: (1) computation of the model phase and  
 308 correction of navigation bit jumps, and (2) inversion of observed signals using FSI to retrieve  
 309 bending angles as a function of impact parameter.

310

### 311 3.2.1 Calculation of model phase

312

313 The model phase is derived from a reference refractivity profile computed using the MSIS\_90  
 314 climatology (Hedin, 1991), assuming 90% relative humidity below 15 km. Refractivity ( $N$ ) is  
 315 calculated as

316

$$317 N = 77.6 \frac{P}{T} + 3.73 \times 10^5 \frac{e}{T^2} \quad (4)$$

318

319 where  $P$  is pressure,  $T$  is temperature, and  $e$  is water vapor. The model impact parameter ( $a$ ) at  
 320 altitude  $z$  is calculated as

321

$$322 a = n(R + z) = nr, \quad (5)$$

323

324 where,  $n = 1 + N \times 10^{-6}$ ,  $R$  is the local radius of curvature of the Earth, and  $r = R + z$ .

325

326 The bending angle ( $\alpha$ ) profile is derived from  $n$  and  $a$  using Abel integration

327

$$328 \alpha(p) = 2p \int_{r1}^{\infty} \frac{a}{\sqrt{n^2 r^2 - a^2}} \frac{d \ln(n)}{dr} dr, \quad (6)$$

329

330 The impact parameter and bending angle profiles, along with occultation time ( $t$ ), satellite  
 331 positions, and velocities, are then used to derive the Doppler shift associated with the  
 332 atmospheric refractivity  $n(z)$ . The model phase, computed from occultation time and the  
 333 Doppler shift, provides a reference for identifying navigation bit jumps.

334

335 In most RO data, navigation bits embedded in the excess phase and coordinate time series can  
 336 introduce discontinuities of  $\pm\pi$ . These phase jumps are identified by comparing the measured  
 337 excess phase with the model phase, especially at high sampling rates ( $\geq 50$  Hz). Once detected,  
 338 the navigation bit pattern is applied to correct discontinuities in the measured phase, ensuring  
 339 continuity and accuracy in the processed phase time series.

340

### 341 3.2.2 Full Spectrum Inversion

342

343 To retrieve bending angles from RO signals, it is essential to reduce high-frequency noise in  
 344 the excess phase. This is typically achieved using low-pass or radio-holographic filters  
 345 (Gorbunov et al., 2005). In the current RFSI inversion system, a 0.5-second low-pass Fourier  
 346 filter is applied to the excess Doppler signal (the time derivative of excess phase). The filtered  
 347 Doppler is then reintegrated to recover a smoothed excess phase. The 0.5-second window  
 348 approximately matches the vertical resolution of RO observations, corresponding to the first  
 349 Fresnel zone (Kursinski et al., 1997). To better resolve fine-scale refractivity structures in the  
 350 lower atmosphere, a shorter, height-dependent smoothing window is used below 10 km: 0.05  
 351 seconds for 100 Hz data and 0.1 seconds for 50 Hz, enabling noise reduction while preserving  
 352 small-scale features. The choice of these parameters is based on systematic tuning experiments  
 353 in which multiple configurations were evaluated. The selected values showed here provide the  
 354 most consistent statistical agreement with model outputs, such as ERA5, yielding reduced  
 355 bending angle bias and standard deviation compared with other tested configurations.

356  
357  
358  
359  
360  
361  
362  
363  
364  
365  
366  
367  
368  
369  
370  
371  
372  
373  
374  
375  
376  
377  
378  
379  
380  
381  
382  
383  
384  
385  
386  
387  
388  
389  
390  
391  
392  
393  
394  
395  
396  
397  
398  
399  
400

Bending angles are computed using geometric optics (GO) above 25 km and the full spectrum inversion method below this altitude. In FSI, the received signal is expressed as a sum of narrowband sub-signals in the open-angle domain  $\theta$ :

$$u(\theta) = \sum_p A_p(\theta) e^{i\varphi_p(\theta)} \quad (7)$$

where,  $A_p$  and  $\varphi_p$  are the amplitude and phase of the  $p$ th sub-signal, respectively. The Fourier transform of Eq. (7) is:

$$F(\hat{\omega}) = \sum_p \int_{\theta_1}^{\theta_2} A_p(\theta') e^{i(\varphi_p - \hat{\omega}'\theta')} d\theta' \quad (8)$$

where  $\theta_1$  and  $\theta_2$  represent the open angles at the start and end of the occultation, respectively.

Applying the method of stationary phase (MSP) (Born and Wolf, 1999; Jensen et al., 2003), the transform simplifies to:

$$F(\hat{\omega}) \approx B e^{i(\varphi_q - \hat{\omega}_q \theta_s)} \quad (9)$$

where  $B$  is an approximately constant amplitude, and the pseudo frequency  $\hat{\omega}_q$  satisfies

$$\hat{\omega}_q = \left. \frac{d\varphi_q}{d\theta} \right|_{\theta=\theta_s} \quad (10)$$

The stationary points  $\theta_s$  is then given by:

$$\theta_s = -\frac{d\psi}{d\hat{\omega}}, \text{ where } \psi = \varphi_q - \hat{\omega}_q \theta_s \quad (11)$$

The derivative of the phase ( $\varphi_q$ ) with respect to  $\theta$ , accounting for the signal path from the GNSS to LEO satellite, is:

$$\frac{d\varphi_q}{d\theta} = \hat{\omega}_q = ka + k \frac{dR_L}{d\theta} \sqrt{1 - \left(\frac{a}{R_L}\right)^2} + k \frac{dR_G}{d\theta} \sqrt{1 - \left(\frac{a}{R_G}\right)^2}, \quad (12)$$

where  $k$  is the wavenumber of the carrier signal,  $R_L$  and  $R_G$  are the distances from the GNSS and LEO satellites to the local center of curvature, respectively, and  $a$  is the impact parameter.

Assuming circular orbits, the derivatives of  $R_L$  and  $R_G$  vanish, reducing Eq. (12) to:

$$\frac{d\varphi_q}{d\theta} = ka \quad (13)$$

Differentiating with respect to  $\hat{\omega}$  gives:

$$da = \frac{1}{k} d\hat{\omega}, \quad (14)$$

The spectral resolution of the Fourier transform phase,  $d\hat{\omega}$ , is given by (Adhikari et al. 2016):

401 
$$d\hat{\omega} = \frac{2\pi}{\Delta\theta}, \text{ where } \Delta\theta = \theta_2 - \theta_1 \quad (15)$$

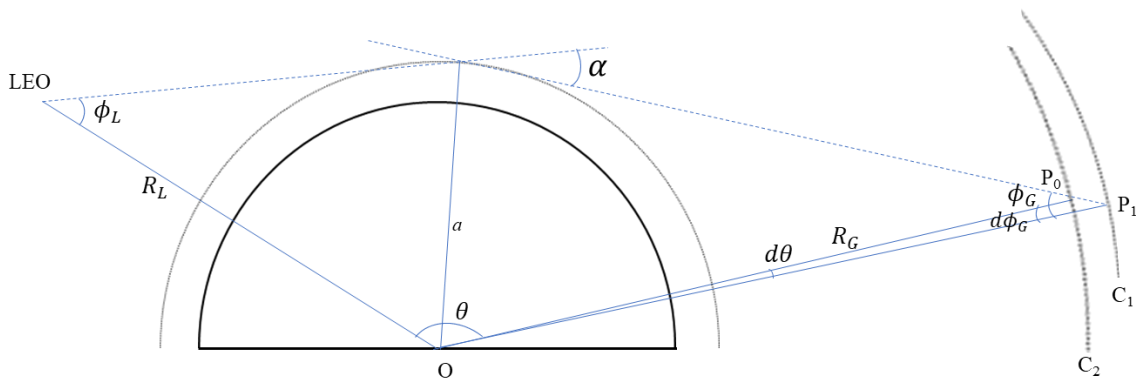
402  
403 Finally, with the impact parameter  $a$  and the open angle  $\theta$ , the bending angle is computed as:  
404

405 
$$\alpha(a) = \theta + \arcsin\left(\frac{a}{R_L}\right) + \arcsin\left(\frac{a}{R_G}\right) - \pi. \quad (16)$$

406  
407 **3.2.3 Correction for non-spherical trajectory**  
408

409 The assumption underlying Eq. (16) is invalid in realistic occultation scenarios due to the  
410 Earth's oblateness and the non-coplanar nature of GNSS and LEO satellite orbits. To account  
411 for these effects, a correction must be applied to the observed phase to project the signal path  
412 onto circular, coplanar trajectories. As illustrated in Fig. 2, the actual GNSS satellite orbit  
413 is represented by arc  $C_1$ , with each point along the trajectory projected onto a circular orbit,  $C_2$ .  
414 Notably, the impact parameter ( $a$ ) remains unchanged during this projection. In this process,  
415 the GNSS position is shifted from  $P_1$  on arc  $C_1$  to  $P_0$  on arc  $C_2$ . This projection alters the open  
416 angle ( $\theta$ ), the signal ray ( $\phi_G$ ), and the phase of the signal. Although Fig. 2 focuses on the GNSS  
417 orbit, the same projection method is also applied to the LEO receiver orbit. Given the known  
418 positions of the GNSS and LEO satellites, the resulting changes in phase and open angles can  
419 be determined geometrically. Note that the radius and center of curvature are treated as fixed  
420 for a given RO event and are not dynamically reprojected. The projection is performed with  
421 respect to the precomputed local center of curvature, ensuring a consistent coordinate system  
422 throughout the inversion process.

423



424  
425 Fig. 2: Projection of a non-circular orbit relative to the local center of curvature to a circular  
426 orbit.

427  
428 After calculating bending angles for the L1 and L2 frequencies separately, the profiles are  
429 truncated using the FSI amplitude. This step is necessary because the FSI method produces  
430 bending angle and impact parameter pairs over an infinite range of impact parameters.  
431 Determining the lowest impact parameter and its corresponding bending angle is critical. In the  
432 current STAR FSI inversion approach, the pair with the lowest impact parameter and bending  
433 angle is identified based on the amplitude of the Fourier transform. The amplitude is first  
434 normalized using the signal's mean amplitude within the 10-50 km range. The lowest point is  
435 defined as the altitude location at which the normalized amplitude the amplitude drops  
436 below 0.35 of the normalized amplitude. This threshold is empirically determined based on  
437 extensive testing within the STAR FSI system. It represents an optimal balance between  
438 maximizing vertical penetration depth and minimizing noise-induced artifacts into the  
439 retrieved bending angle profile.

440  
441  
442

### 3.2.4 Bending Angle Uncertainty Calculation

443 The uncertainty in the bending angle is estimated using a sliding spectrogram with a 500 m  
444 window. First, a smoothed bending angle profile is generated to identify the central component.  
445 Then, the bending angle from the unsmoothed signal is calculated at 1 m impact height  
446 resolution. With each spectral window, deviations from the central component are used to  
447 construct a local power spectrum of the shifted bending angle, computed using a finite bending  
448 angle increment ( $\delta\alpha = 0.0005$  rad). The shifted bending angle ( $\alpha_s$ ), is defined as the  
449 instantaneous bending angle minus the central component. The spectral width ( $\Delta s$ ) is  
450 determined as the mean of the absolute value of the shifted bending angle ( $\alpha_s$ ) weighted by the  
451 spectral power ( $\rho$ ) of each component, as follows:

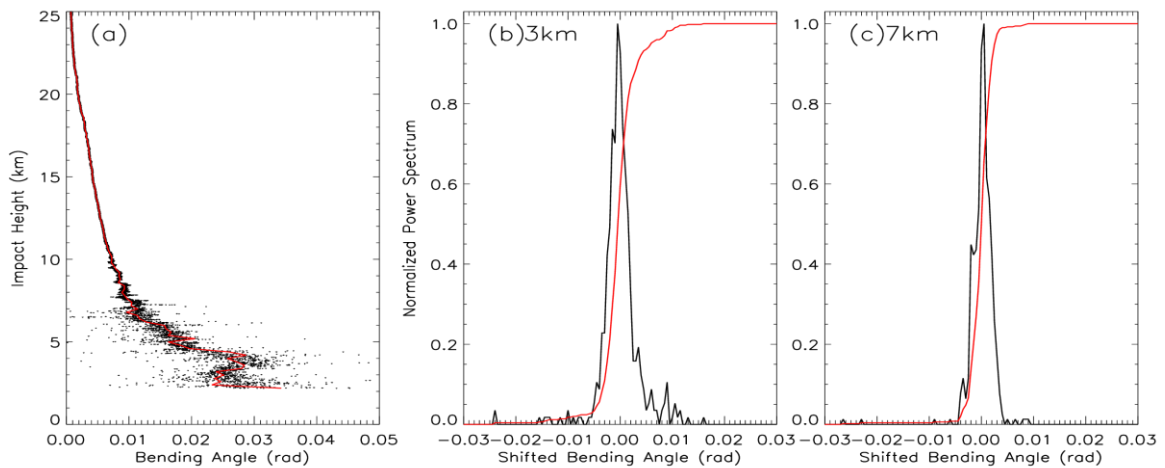
452

$$\Delta s = \sqrt{\frac{\sum_{i=1}^n \rho_i \alpha_s^2 \delta\alpha}{\sum_{i=1}^n \rho_i \delta\alpha}} \quad (17)$$

454

455 Figure 3(a) presents a representative bending angle profile at 1 m resolution as a function of  
456 the impact height (black dots), along with its central component (red line). Figure 3(b) and 3(c)  
457 show the corresponding normalized power spectrum (black line) and accumulated power  
458 spectrum (red line) at impact heights of 3 km and 7 km, respectively. As illustrated, the spectral  
459 range at 3 km is broader than at 7 km, indicating greater atmospheric variability at lower  
460 altitudes. The bending angle uncertainty is quantified as half the spectral width, calculated  
461 using Eq. (17).

462



463

464 Fig. 3: (a) Spectrogram of the RO signal, power spectrum at (b) 3 km, and (c) 7.5 km impact  
465 heights.

466

### 3.3 Bending angle Inversion

467

#### 3.3.1 Ionospheric Correction and Optimization

468

469 To remove first-order ionospheric effects, and as an approximation for the neutral atmosphere  
472 bending angle, a linear combination of L1 and L2 bending angles ( $\alpha_1(a)$  and  $\alpha_2(a)$ ) is  
473 computed (Vorob'ev and Krasil'nikova, 1994):

474

$$\alpha_{LC}(a) = \frac{\alpha_1(a)f_1^2 - \alpha_2(a)f_2^2}{f_1^2 - f_2^2} \quad (18)$$

475

476  
477 where  $f_1$  and  $f_2$  are the RO frequencies.

478  
479 This is followed by statistical optimization (Gorbunov, 2002c):

480  
481 
$$\alpha(a) = \alpha_{BG}(a) + \frac{\sigma^S}{\sigma^S + \sigma^N} (\alpha_{LC}(a) - \alpha_{BG}(a)) \quad (19)$$

482  
483 where,  $\sigma^S$  and  $\sigma^N$  are the covariances of the neutral atmospheric signal and residual noise,  
484 respectively, and  $\alpha_{BG}(a)$  is the background bending angle from a climatological model ([MSIS-](#)  
485 [90 model](#)).

486  
487 Covariance matrices are estimated from the deviation ( $\Delta\alpha$ ) of L1 and L2 bending angles from  
488 the background model ( $\alpha_{L1,L2} - \alpha_m$ ). For ionospheric signal and noise, deviations in the impact  
489 heights (impact parameter minus local center of curvature) of 50-70 km are used; for neutral  
490 atmospheric signal, the 12-35 km range is used. In the lower troposphere, near the surface,  
491 where the L2 signals weaken, a constant correction is applied based on the lowest valid L2  
492 altitude.

### 493 494 **3.3.2 Abel Inversion**

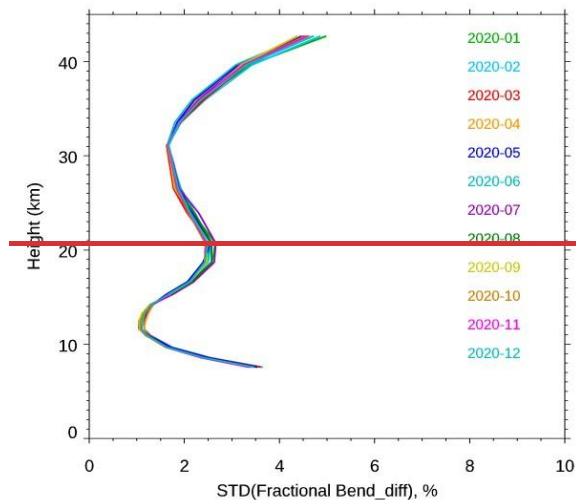
495  
496 Refractivity is retrieved from ionosphere-corrected bending angles using the Abel transform  
497 (Fjeldbo et al., 1971). The bending angle profile is extended up to 150 km using climatological  
498 data ([MSIS-90 model](#)) to stabilize the upper boundary condition. Tangent point locations are  
499 recovered by interpolating the occultation time and satellite positions. Since time information  
500 is lost during the Fourier transform of the RO signal, the occultation time is reconstructed from  
501 the bending angle-impact parameter profile and used to infer the latitude and longitude of each  
502 tangent point.

### 503 504 **3.4 Quality control**

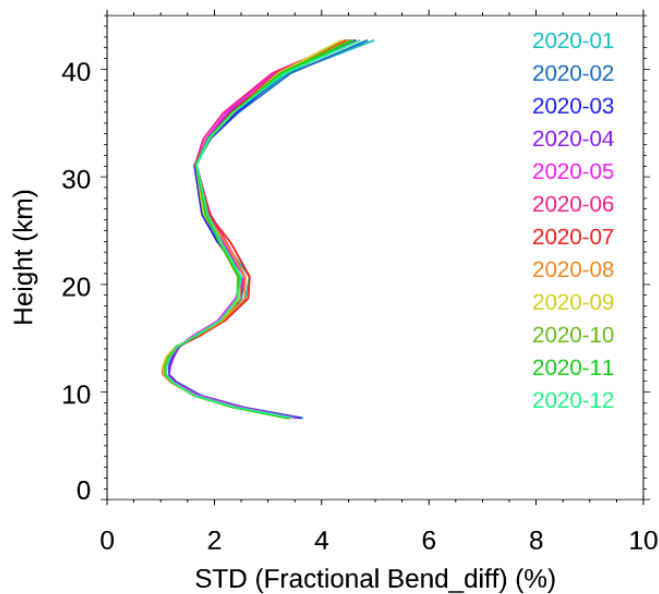
505  
506 Due to the lack of effective internal quality control in the ROPP v10 package, we rely on  
507 external quality control procedures to identify bad profiles. The fractional difference between  
508 the observed (O) and simulated (B) bending angles, calculated from ERA5 forecast fields, is  
509 used to assess the quality of the RO data at each altitude level:

510  
511 
$$BA_{diff} = \frac{O-B}{B} \quad (20)$$

512  
513 Figure 4 shows the monthly mean standard deviation of the fractional bending angle  
514 differences for 2020, from 8 to 43 km altitude. The annual mean standard deviation ( $\sigma_{year}$ ) is  
515 used as a benchmark. A profile is flagged as ‘bad’ if the bending angle difference exceeds  $7\sigma_{year}$   
516 at any altitude level between 10 and 40 km, where RO data quality is highest and model-  
517 observation agreement is strongest. A sensitivity study confirmed that using a  $7\sigma$  year threshold  
518 provides an optimal balance between data retention and data quality.



519



520

521 Fig. 4. Monthly standard deviation of the fractional bending angle differences in 2020.

522

523 In addition, profiles are also flagged as ‘bad’ under any of the following conditions: ~~(1) Model~~  
 524 ~~simulation data is unavailable;~~ (21) The fractional BA difference exceeds  $7\sigma_{years}$ ; ~~(32)~~ The top  
 525 height of the profile is below 20 km; (43) The bottom height is above 20 km; and (54) A  
 526 negative bending angle is detected below 50 km. The QC rejection rate for the ROMEX dataset  
 527 depends on the mission. For example, the QC pass rates are 85.7%, 94.8%, and 93.9% for  
 528 COSMIC-2, Spire, and PlanetiQ, respectively. These values are comparable to those from  
 529 CDAAC-processed data: 87.6%, 95.7%, and 90.6%, respectively.

530

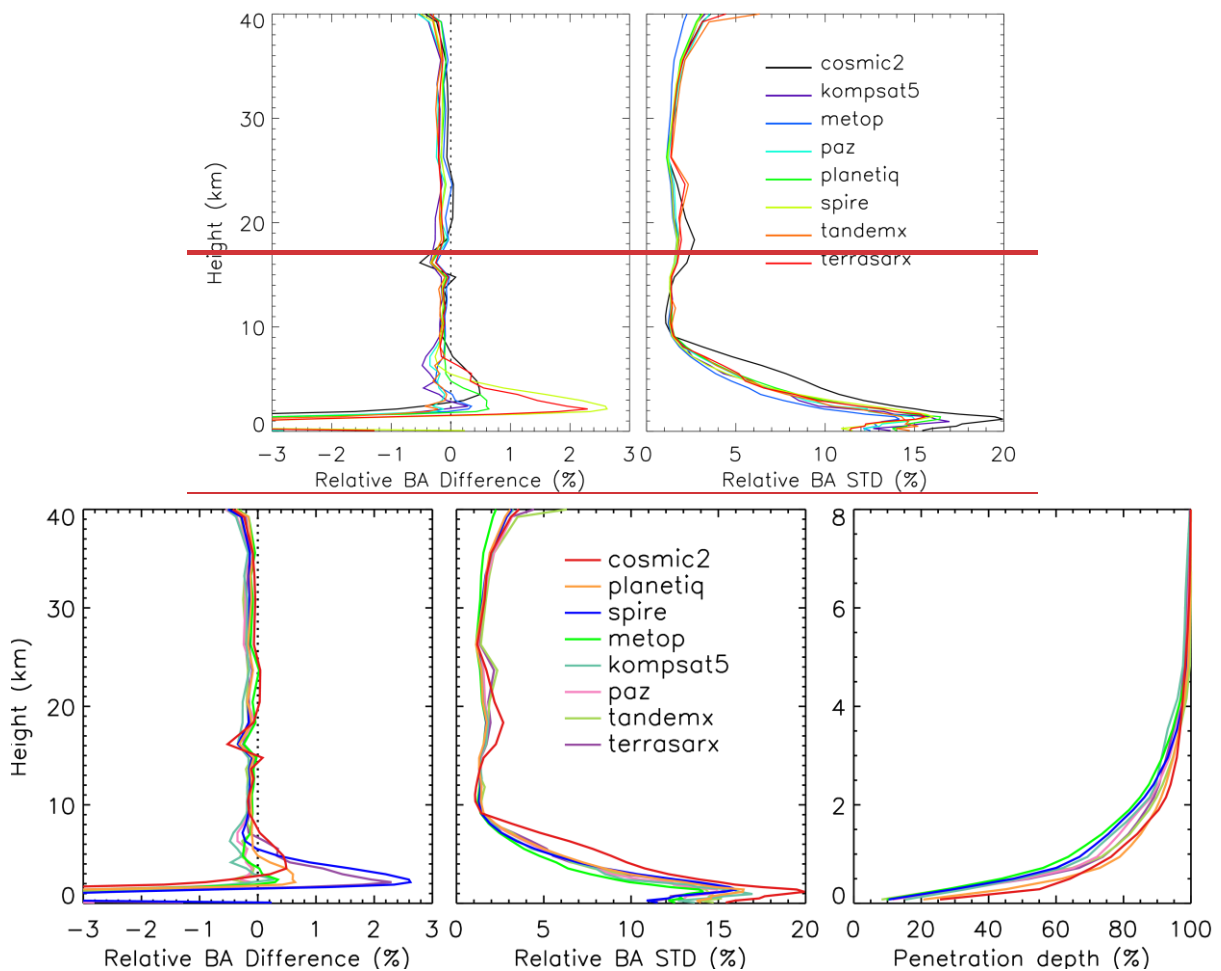
531 It is important to note that this quality control procedure applies only to bending angles within  
 532 a specific height range (10-40 km). In rare cases, even when the bending angle passes QC,  
 533 anomalies in refractivity or dry temperature may still occur due to limitations in the Abel  
 534 inversion. Future updates to the QC procedures will address such issues. This process ensures  
 535 that only high-quality profiles are retained as valid. An internal quality control system tailored  
 536 for near-real-time processing is under development; however, it was not incorporated into the  
 537 ROMEX data when that dataset was produced.

538  
 539  
 540  
 541  
 542  
 543  
 544  
 545  
 546  
 547  
 548  
 549

## 4. Comparison Results

### 4.1 Bending angle comparison with STAR RFSI, STAR ROPP, and EUMETSAT

Figure 5 shows the height-dependent fractional bending angle differences between RO observations and ERA5 background fields (O-B) for multiple satellite missions processed using the RFSI algorithm during November 2022. The selected missions include COSMIC-2, Spire, PlanetiQ, Metop-B, Metop-C, Kompsat5, PAZ, TerraSAR-X, and TanDEM-X. The comparison serves as a proxy for evaluating the quality and inter-mission consistency of RFSI-processed RO data relative to a widely used global reanalysis.



550  
 551  
 552  
 553  
 554  
 555  
 556  
 557  
 558  
 559  
 560  
 561  
 562  
 563

Fig. 5. Comparison of height-dependent fractional bending angle between RO observations and ERA5 simulations (O-B) among different RO missions. BA mean biases (left), and standard deviations (right middle) in terms of fractional BA difference (%), and (right) penetration depth below 8 km for RFSI over November 2022.

In the middle and upper troposphere through the lower stratosphere (8-35 km), all missions exhibit excellent agreement with ERA5. Mean O-B differences are generally within  $\pm 0.2\%$ , and standard deviations remain below 3%, indicating high internal consistency among the RO datasets and strong alignment with ERA5 in this well-observed atmospheric region.

In the lower troposphere (below 8 km), larger biases and variability are evident, especially near the surface. Spire and TerraSAR-X show mean biases up to 1-2% at 2 km, with standard

564 deviations exceeding 10%. COSMIC-2 exhibits the highest variability in this region, with  
565 standard deviations approaching 20% at approximately 1 km. These discrepancies are likely  
566 attributed to increased atmospheric variability in the lower troposphere boundary layer,  
567 limitations in signal tracking during multipath propagation at tropical/subtropical regions  
568 where high water vapor variability makes OL tracking difficult, and the sensitivity of bending  
569 angle retrievals to SNR cut-off thresholds. In contrast, PlanetiQ, Metop-B, and Metop-C  
570 demonstrate smaller near-surface biases (typically <0.5%) and reduced variability, suggesting  
571 robust signal tracking and/or more effective pre-processing of low-altitude data.

572

573 Above 35 km, mean biases increase to approximately 0.6%, and standard deviations increase  
574 with height and can exceed 5% at 40 km. These deviations are primarily due to limitations in  
575 ionospheric correction at higher altitudes, where residual ionospheric effects are more  
576 challenging to remove completely. The ionospheric conditions during September-November  
577 2022 were generally moderate and typical for the ascending phase of Solar Cycle 25, but  
578 intermittently disturbed (including several geomagnetic storms and enhanced irregularities).  
579 They are not representative of worst-case conditions, but also not purely quiet-average; they  
580 are better described as moderately active with episodic disturbances.

581

582 Among the evaluated missions, PlanetiQ consistently shows low mean biases and standard  
583 deviations across nearly the entire vertical range, indicating strong data stability and processing  
584 robustness. Metop-B and Metop-C also exhibit excellent performance, likely due to mature  
585 sensor platforms and the use of well-established pre-processing procedures in the ROPP  
586 system. Spire data, while reliable in the mid- to upper troposphere, shows elevated near-surface  
587 variability, likely due to its higher sensitivity to excess phase pre-processing (e.g., cycle-slip  
588 removal and parameter tuning).

589

590 COSMIC-2 displays distinct behavior relative to other missions, with positive biases of 8-35  
591 km and increased variability near the tropopause. These features are likely influenced by its  
592 low-inclination orbit and limited latitudinal coverage ( $\pm 45^\circ$ ), which concentrates observations  
593 in tropical and subtropical regions with higher atmospheric variability. Similar features and  
594 their impact on data assimilation performance have been discussed in previous studies (Ho et  
595 al., 2023; Miller et al., 2025).

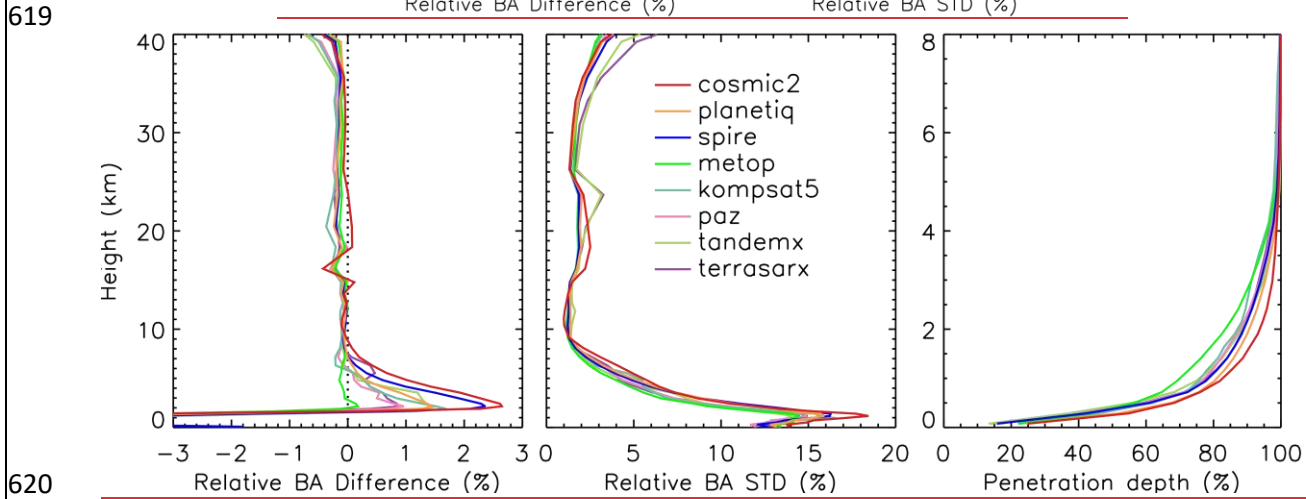
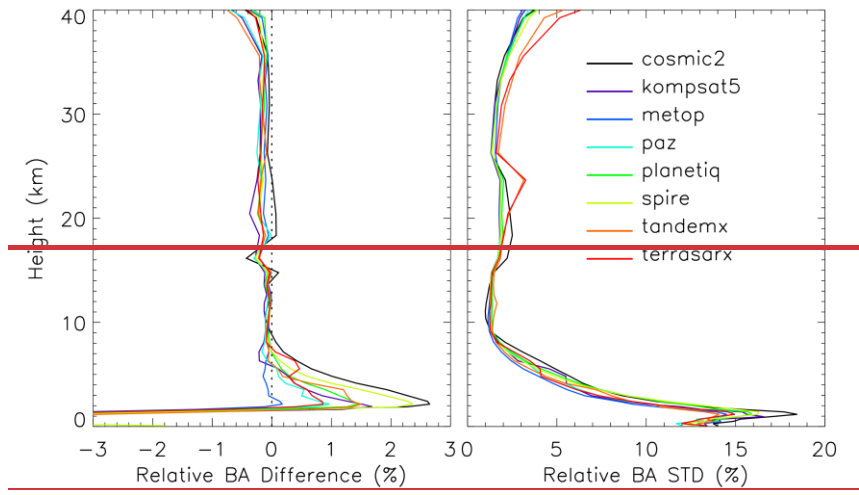
596

597 The penetration depth is defined as the minimum height above ground level where a valid (i.e.,  
598 not filled or missing) bending angle or refractivity is obtained for a given RO event. Smaller  
599 penetration depths indicate that the RO signal reaches closer to the Earth's surface. Penetration  
600 depth depends on the signal cutoff criteria applied during processing (see Sections 3.1 and  
601 3.2.3); therefore, comparisons among different missions should be made using the same  
602 processing center and algorithm. The right panel of Figure 5 shows the penetration depth  
603 profile below 8 km, expressed as the percentage of profiles reaching different altitudes relative  
604 to 8 km, for the FSI method. As discussed by Gorbunov et al. (2022a, 2022b), higher SNR  
605 generally improves tropospheric penetration. Consistent with Table 2, COSMIC-2 and  
606 PlantiQ exhibit the greatest penetration depth among the missions. Most missions achieve  
607 more than 80% of occultations reaching 2 km or lower, and more than 50% reaching 1 km or  
608 lower. The penetration depths are noticeably higher for Metop-B and Metop-C (green line),  
609 while Spire, despite having the lowest SNR, achieves a slight better penetration than Metop.

610

611 Figure 6 shows O-B bending angle differences for the same missions and period, but with data  
612 processed using the ROPP-CT2 method. The vertical structure of mean biases and variability  
613 is broadly similar to that in the RFSI results, reflecting consistent retrieval behavior between

614 the two approaches. In the 8-35 km range, both methods yield small biases (within  $\pm 0.2\%$ ) and  
 615 standard deviations below 3%, confirming the reliability of both retrievals in the core  
 616 atmospheric region. One exception is KOMPSAT-5, which shows a slight negative bias ( $\sim$   
 617  $-0.2\%$ ) between 17 and 23 km.  
 618



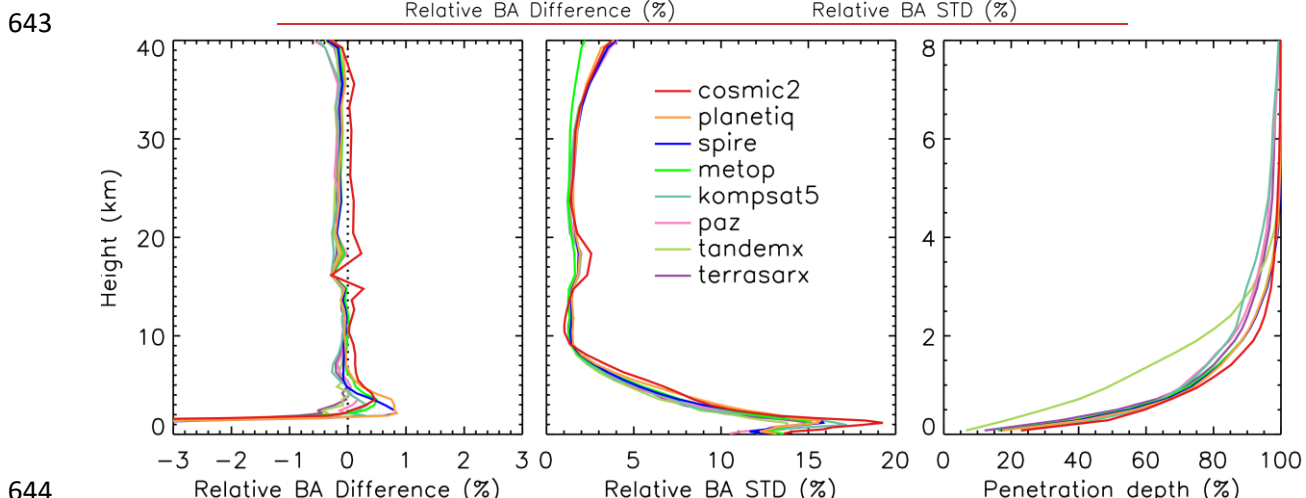
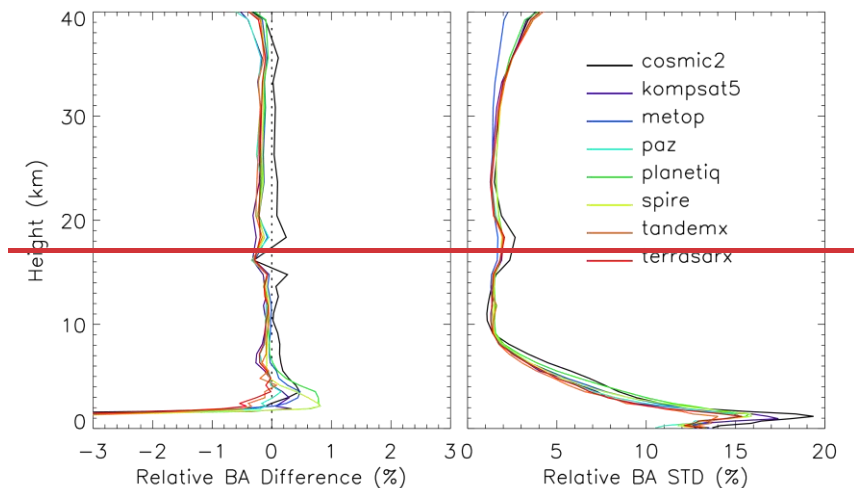
621 Fig. 6. Same as Fig. 5, but for RO data generated from the ROPP package using the CT2  
 622 method.

623  
 624 Standard deviations increase above 35 km and below 8 km in both datasets, highlighting  
 625 common challenges in the upper and lower atmospheric regions, including multipath effects,  
 626 signal noise, and uncertainty in ionospheric corrections. However, the CT2 retrievals generally  
 627 exhibit larger near-surface biases than those of RFSI. For all missions except Metop-B and  
 628 Metop-C, the CT2-processed profiles exhibit biases of 1-2% near the surface, likely due to the  
 629 more conservative use of signals and stronger smoothing.

630  
 631 In contract to Fig. 5, the penetration depth profiles among missions are much narrower below  
 632 1 km, indicating that CT2 is less sensitive to SNR. Consistent with Fig. 5, COSMIC-2 and  
 633 PlanetiQ show the deepest penetration depth among the missions. The penetration depths are  
 634 noticeably higher for Metop-B and Metop-C than for Spire.

635  
 636 Figure 7 displays ERA5 O-B differences for RO profiles processed by EUMETSAT, covering  
 637 the same missions and period. Like the other two datasets, EUMETSAT results show high  
 638 consistency in the 8-35 km range, with mean biases within  $\pm 0.2\%$  and standard deviations  
 639 below 3%. COSMIC-2 again stands out, showing a positive bias of  $\sim 0.2\%$ , while most other

640 missions exhibit slightly negative biases, suggesting a systematic offset in COSMIC-2 data  
 641 relative to the ensemble.  
 642



644  
 645 Fig. 7. Same as Fig. 5, but for RO data provided from EUMETSAT.

646  
 647 In the lower troposphere, EUMETSAT retrievals exhibit the smallest mean biases (<1% at 2  
 648 km) among the three datasets, suggesting more effective mitigation of noise and multipath  
 649 effects near the surface. By comparison, RFSI-processed profiles for Spire and TerraSAR-X  
 650 show near-surface biases of up to ~2%, while CT2 retrievals yield 1-2% biases for most  
 651 missions. COSMIC-2 exhibits high variability below 8 km across all three datasets, although  
 652 the CT2 method appears to reduce it slightly.

653  
 654 Above 35 km, the bending angle uncertainty increases in all datasets. However, EUMETSAT  
 655 results exhibit more uniform performance across missions, with mean biases generally below  
 656 0.5% and smaller inter-mission variability. Metop-B and Metop-C show the lowest standard  
 657 deviations across all datasets in this altitude range, indicating highly stable performance at high  
 658 altitudes.

659  
 660 The penetration depth from TanDEM-X is noticeably higher than that of other missions in the  
 661 EUMETSAT-processed data. For Metop-B and Metop-C, penetration depths are substantially  
 662 improved compared with STAR FSI and STAR ROPP CT2, and approach those of COSMIC-  
 663 2 and PlanetiQ below 1.5 km.

664

665 Together, these intercomparisons highlight key trade-offs among the different retrieval  
666 approaches. The RFSI method leverages the full frequency content of the RO signal, offering  
667 enhanced sensitivity to fine-scale atmospheric features. However, it is also more sensitive to  
668 noise, particularly near the surface. In contrast, the CT2 method employs a canonical  
669 transformation that simplifies retrieval but is more conservative in its use of signal data,  
670 resulting in smoother profiles and slightly larger near-surface biases. EUMETSAT's  
671 processing strikes a balance between these extremes, achieving consistent results across the  
672 full vertical range while effectively suppressing noise in the lower troposphere and upper  
673 stratosphere.

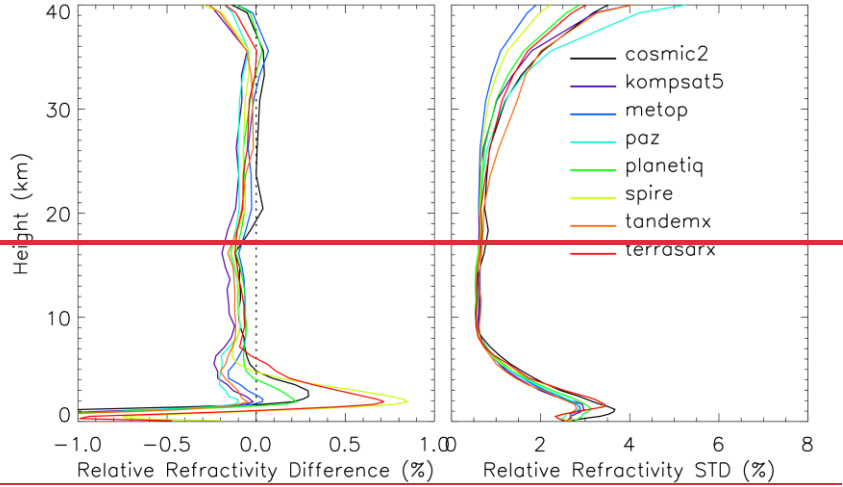
674

#### 675 **4.2 Refractivity comparison with STAR RFSI, STAR ROPP, and EUMETSAT**

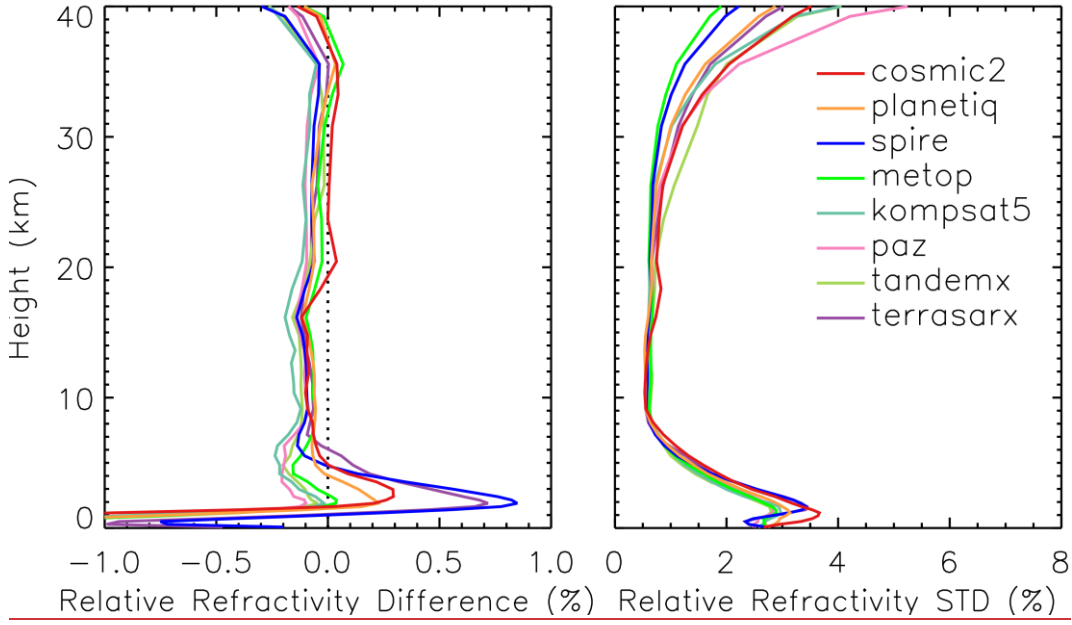
676

677 Figure 8 presents the fractional refractivity differences between RO observations processed  
678 using the RFSI algorithm and ERA5 background fields for November 2022. The vertical  
679 structures of refractivity O-B statistics largely mirror those of the bending angle differences  
680 shown in Fig. 5, reflecting the propagation of bending angle quality into the refractivity  
681 retrieval. In the well-constrained 8-30 km region, all missions show excellent agreement with  
682 ERA5. Mean biases remain within  $\pm 0.15\%$ , and standard deviations are typically below 1%,  
683 indicating that refractivity retrievals in this core region retain the stability and consistency of  
684 the underlying bending angle data.

685



686



687

688 Fig. 8. Comparison of height-dependent fractional refractivity between RO observations and  
 689 ERA5 simulations (O-B) among different RO missions. Refractivity mean biases (left) and  
 690 standard deviations (right) in terms of fractional difference (%) for RFSI over November 2022.

691

692

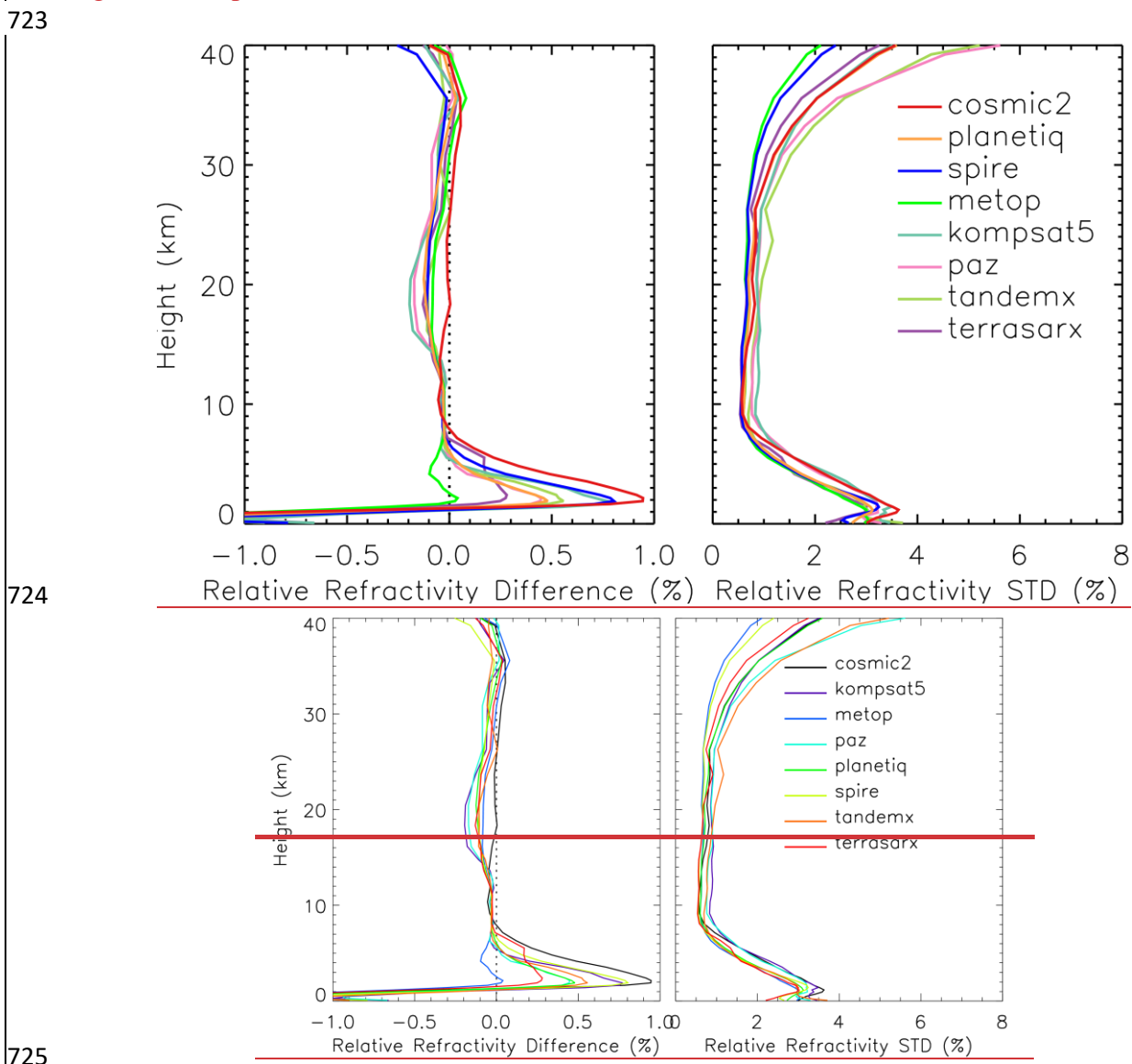
693 In the lower troposphere (below ~8 km), refractivity differences exhibit a significantly larger  
 694 inter-mission spread, consistent with Fig. 5, although both biases and standard deviations are  
 695 generally reduced. Spire and TerraSAR-X exhibit the most pronounced positive biases,  
 696 reaching ~0.7-0.8% near 2 km, along with elevated standard deviations exceeding 3%.  
 697 COSMIC-2 again exhibits high variability below 5 km, with standard deviations peaking at  
 698 over 3.5% near 1 km. However, its mean refractivity bias remains relatively small compared  
 699 to those from Spire or TerraSAR-X, suggesting increased random error rather than systematic  
 700 offset.

701

702 In the upper atmosphere (above ~35 km), where refractivity is less sensitive to the RO signal  
 703 due to the exponential decrease in atmospheric density, the mean biases for all missions begin  
 704 to increase negatively, reaching values of ~-0.2% to -0.4% near 40 km. Standard deviations  
 705 also rise, ranging from ~2% to 5%, consistent with the increased variability observed in the  
 706 bending angle differences shown in Fig. 5. These errors are primarily attributed to residual

707 ionospheric correction uncertainties and the influence of high-altitude extrapolation  
 708 assumptions in the RFSI algorithm. The use of climatological models in the upper atmosphere  
 709 also introduces additional variability, as refractivity becomes more sensitive to model  
 710 inaccuracies in this region.

711  
 712 Figure 9 shows the refractivity O-B differences derived from RO data processed with the ROPP  
 713 CT2 method. Between 8 and 15 km, CT2 results exhibit improved inter-mission consistency  
 714 in mean bias compared to RFSI, although the standard deviations are generally larger. In the  
 715 lower troposphere (below ~8 km), CT2 retrievals produce larger positive biases, typically  
 716 around 0.5-1% near 2 km (except for Metop-B, Metop-C, and TerraSAR-X), with the largest  
 717 bias observed for COSMIC-2 (~1%). These biases are notably larger than those from RFSI,  
 718 which remain below 0.3% for most missions, except for Spire and TerraSAR-X. Between 15-  
 719 25 km, the CT2 results show a greater inter-mission spread in both mean bias and standard  
 720 deviation compared to RFSI. Above 25 km, CT2 and RFSI show broadly similar behavior,  
 721 with rising uncertainty consistent with bending angle trends. Note that both RFSI and CT2 used  
 722 geometric optics method above 25 km.

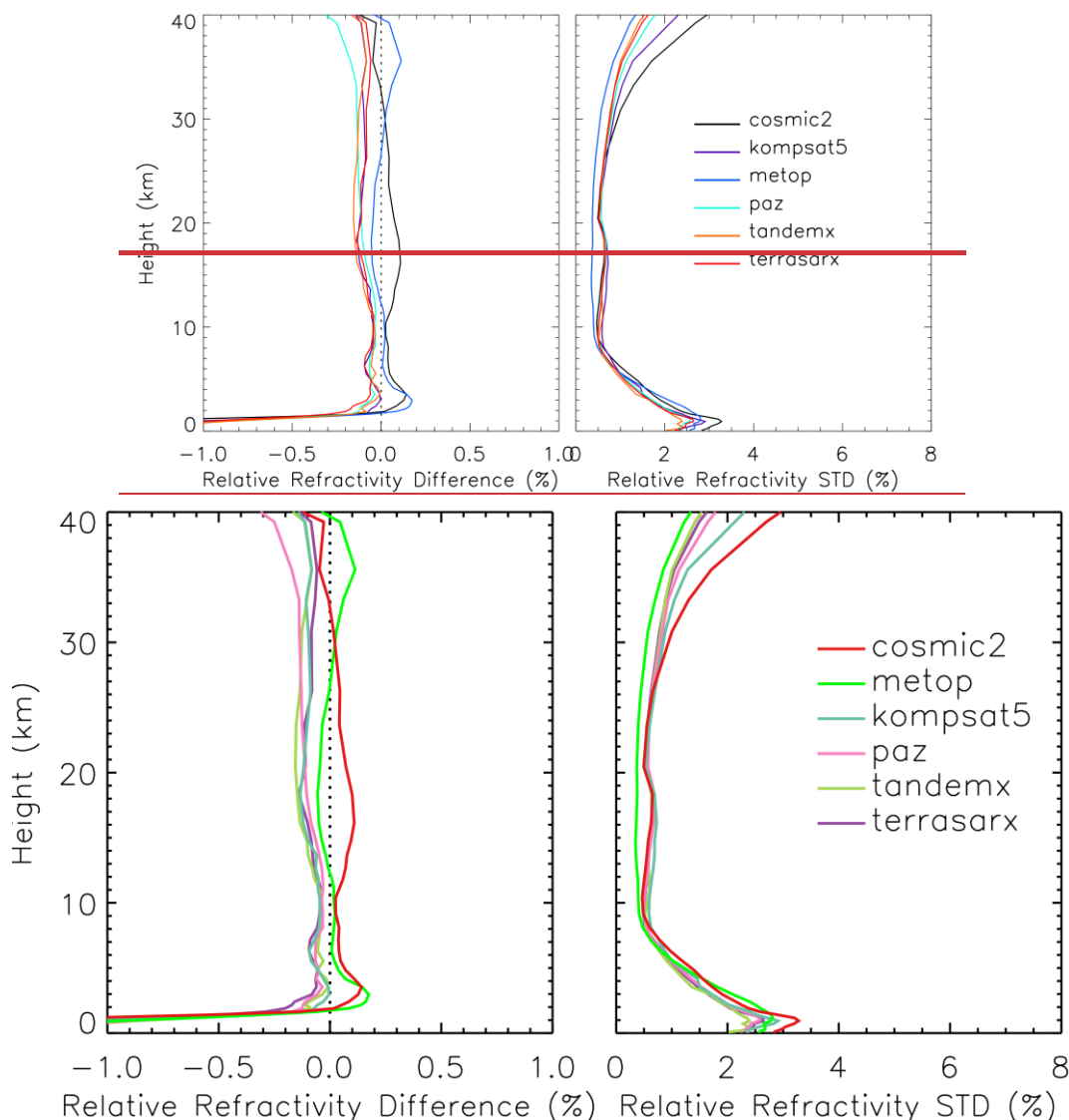


726 Fig. 9. Same as Fig. 8, but for RO refractivity processed using the ROPP package with the CT2  
 727 method.

728  
 729  
 730  
 731  
 732  
 733  
 734  
 735  
 736  
 737  
 738

Figure 10 presents the refractivity O-B differences from the EUMETSAT dataset. Note that refractivity profiles are not available for PlanetiQ and Spire in this dataset. Similar to bending angle results, COSMIC-2 exhibits a distinct positive bias in the 4-30 km region, along with a notably larger inter-missions spread in the 8-40 km range compared to CT2 (Fig. 9) and RFSI (Fig. 8) results. In contrast, in the lower troposphere (below ~8 km), the EUMETSAT retrievals show the smallest near-surface mean biases, generally within  $\pm 0.2\%$  above 2.5 km, and the lowest standard deviation across all available missions. These results suggest that the refractivity data from EUMETSAT are particularly effective at mitigating noise and multipath effects near the surface.

739



740

Fig. 10. Same as Fig. 8, but for RO data provided from EUMETSAT. Note that refractivity data is not available in the EUMETSAT dataset for PlanetiQ and Spire.

741  
 742  
 743  
 744  
 745  
 746  
 747  
 748

Taken together, the comparisons between Figs. 5 and 8, Figs. 6 and 9, and Figs. 7 and 10 reveal that many mission-specific features observed in bending angle retrievals persist in the refractivity domain. This reinforces the importance of bending angle quality, particularly near the surface and in the upper atmosphere, for achieving accurate refractivity retrievals. The heightened sensitivity of refractivity to small-scale errors at the profile boundaries also

749 underscores the need for robust quality control, optimized signal tracking, and careful  
750 algorithm design in future RO missions and processing systems.

751

### 752 4.3 Structural Uncertainty among Different Processing Methods

753

754 Figures 11-15 illustrate the structural bending angle uncertainty associated with the ROPP  
755 (CT2), RFSI, and EUMETSAT processing algorithms for five representative GNSS RO  
756 missions: COSMIC-2, Spire, PlanetiQ, Metop-B, and Metop-C. For each mission, the figure  
757 shows the height-dependent relative mean differences and standard deviations of bending  
758 angles with respect to the three-dataset mean, along with the number of common profiles  
759 processed for each algorithm.

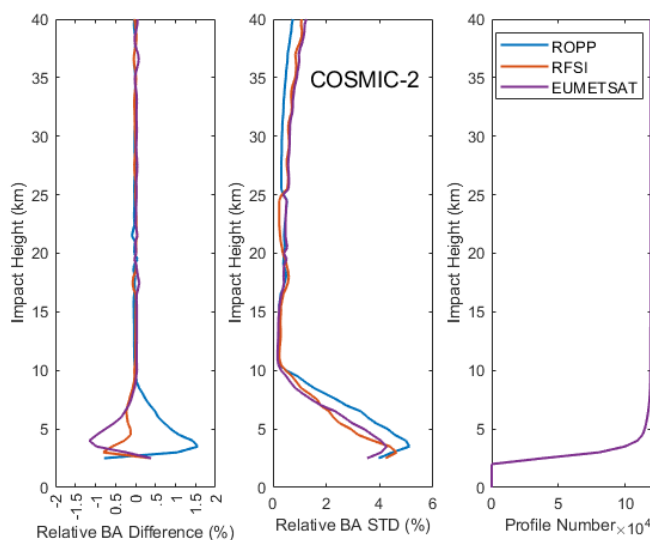
760

761 Several important structural differences emerge from these comparisons:

762

763 For COSMIC-2 (Fig. 11), the three processing methods demonstrate strong consistency in the  
764 middle and upper troposphere and stratosphere (above  $\sim 10$  km), where both the relative  
765 differences and standard deviations of bending angles remain below approximately 0.1% and  
766 1%, respectively, indicating minimal structural uncertainty. Below 10 km, method-dependent  
767 differences become more pronounced. The largest deviations are observed near the surface,  
768 with relative differences of approximately 1.5% for ROPP, -1.0% for EUMETSAT, and -0.5%  
769 for RFSI. Additionally, the ROPP algorithm exhibits higher bending angle standard deviations  
770 in the lowest 10 km, indicating greater sensitivity to retrieval ambiguities under conditions of  
771 multipath propagation. In contrast, above 25 km, ROPP shows slightly lower standard  
772 deviations than RFSI and EUMETSAT. Despite these lower-tropospheric differences, the  
773 overall structural agreement among the three COSMIC-2 processing methods is robust.  
774 Although the number of available profiles (right panel) decreases significantly near the surface,  
775 sufficient observations are present throughout the vertical domain to enable meaningful  
776 statistical comparisons.

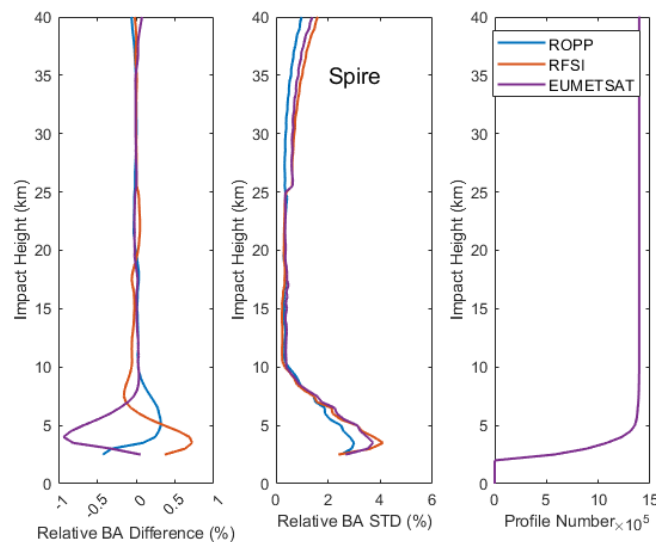
777



778 Fig. 11. Structural bending angle uncertainty among different processing methods for  
779 COSMIC-2. Note that the bending angle profiles from the EUMETSAT dataset are processed  
780 by the UCAR CDAAC using the phase-matching method.

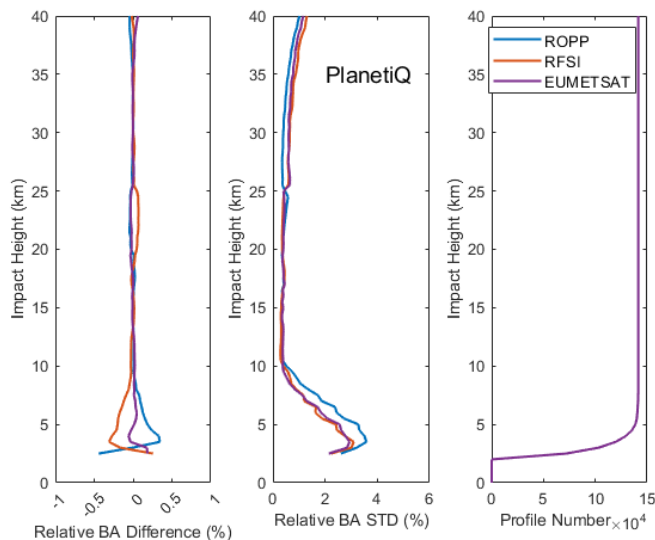
781 For Spire (Fig. 12), a similar pattern of agreement is observed. Above approximately 10 km,  
782 the relative bending angle differences across the three methods are generally within  $\pm 0.1\%$ ,  
783 and the standard deviations remain below 1% up to approximately 35 km, indicating good

784 consistency in the upper atmosphere. However, RFSI exhibits a distinct pattern in the 8-25 km  
 785 range, with a relative positive difference in the 19-25 km region and a negative difference in  
 786 the 8-19 km region, compared to the nearly identical ROPP and EUMETSAT solutions. As  
 787 with COSMIC-2, larger discrepancies emerge below 10 km. Notably, the ROPP and RFSI  
 788 solutions show small positive differences near the surface (up to  $\sim 0.7\%$  and  $\sim 0.3\%$ ,  
 789 respectively), whereas the EUMETSAT solution exhibits a negative deviation of up to  $-1.0\%$ .  
 790 The bending angle standard deviations in the lower troposphere are higher for RFSI and  
 791 EUMETSAT, reaching  $\sim 4\%$ , while ROPP shows slightly lower variability (below  $3\%$ ) near  
 792 the surface. Above 25 km, ROPP again yields lower standard deviations compared to the other  
 793 two methods, consistent with the COSMIC-2 results.



794 Fig. 12. Same as Fig. 11, but for Spire.  
 795  
 796

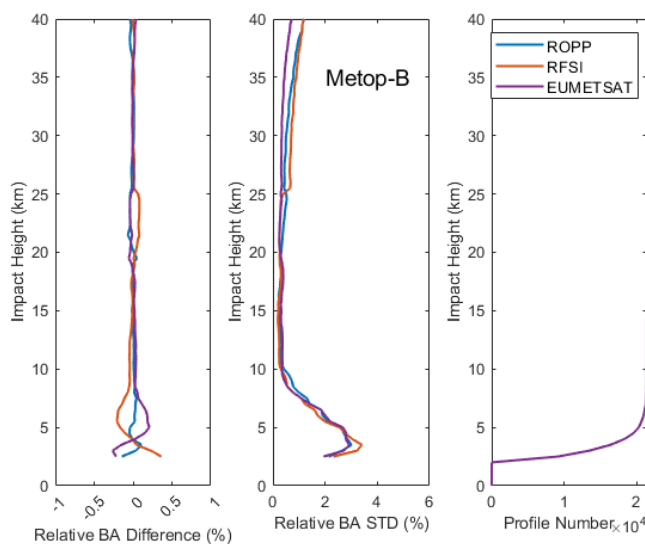
797 For PlanetiQ (Fig. 13), a higher level of consistency is observed among the three processing  
 798 methods across the vertical profile compared to those from COSMIC-2 and Spire. Above  
 799  $\sim 10$  km, the solutions are nearly identical, except for a slight positive deviation in the 19–25 km  
 800 region from the RFSI solution. Relative bending angle differences remain within  $\pm 0.05\%$ , and  
 801 standard deviations are below  $1\%$  up to  $\sim 38$  km, indicating excellent agreement in the middle  
 802 and upper atmosphere. Below 10 km, small but systematic differences become evident. The  
 803 ROPP solution shows a modest positive bias, peaking at approximately  $+0.4\%$  near a 3 km  
 804 impact height, while the RFSI solution exhibits a slight negative bias of similar magnitude.  
 805 The EUMETSAT data remain close to zero throughout this region. As with COSMIC-2, the  
 806 standard deviations increase toward the surface, with ROPP exhibiting greater variability  
 807 below 10 km than RFSI and EUMETSAT. However, for PlanetiQ, the overall variability is  
 808 lower, reaching a standard deviation of  $\sim 3\%$  near the surface. This improved consistency  
 809 suggests enhanced robustness in PlanetiQ's onboard processing, a more stable tracking  
 810 geometry and antenna design, and larger higher SNR, which may reduce sensitivity to  
 811 differences among retrieval algorithms s-differences.



812  
813 Fig. 13. Same as Fig. 11, but for PlanetiQ.  
814

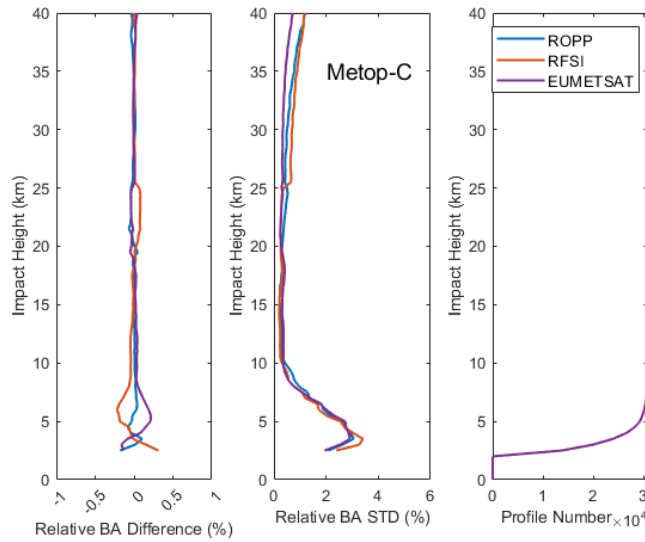
815 Metop-B (Fig. 14) and Metop-C (Fig. 15), both long-operational polar-orbiting satellites with  
816 mature and well-characterized instrumentation, exhibit nearly identical inter-method structural  
817 uncertainties. For brevity, the discussion here focuses on Metop-B. While broad similarities  
818 exist across the three processing methods, structural differences are more pronounced for  
819 Metop-B than for the highly consistent PlanetiQ results. Below an impact height of  $\sim 8$  km, the  
820 standard deviation profiles from all three algorithms converge closely, indicating similar  
821 variability near the surface. Relative bending angle differences show a maximum positive  
822 deviation of approximately  $+0.2\%$  for the EUMETSAT solution and a negative deviation of  
823 about  $-0.2\%$  for RFSI near 5 km.

824  
825 In contrast, the ROPP solution remains close to zero. A slight negative bias is also observed in  
826 the RFSI solution below  $\sim 13$  km ( $\sim -0.1\%$ ). In the upper stratosphere, above 25 km, a clear  
827 separation in variability emerges: RFSI exhibits the largest standard deviations, followed by  
828 ROPP, with EUMETSAT showing the lowest variability. This divergence suggests that the  
829 upper-atmospheric retrievals are more sensitive to processing methodology in the case of  
830 Metop-B.



831

832 Fig. 14. Same as Fig. 11, but for Metop-B.  
 833



834 Fig. 15. Same as Fig. 11, but for Metop-C.  
 835  
 836

837 Except for COSMIC-2, RFSI shows a small positive bias ( $<0.1\%$ ) at 20–25 km for Spire,  
 838 PlanetiQ, and Metop-B/C relative to STAR ROPP and EUMETSAT. Possible causes include  
 839 spectral windowing and filtering choices, as RFSI applies a sliding polynomial filter below 25  
 840 km and an optimal estimation filter above 25 km, which can introduce systematic offsets.  
 841 Degraded L2 signals and reduced GNSS SNR at above  $\sim 20\text{--}25$  km further amplify noise, and  
 842 because FSI is more noise-sensitive than geometric optics or canonical transform methods,  
 843 incomplete noise suppression may yield small positive biases. The exact causes are under  
 844 active investigation to further mitigate this effect.

845  
 846 These results highlight that structural uncertainty is both algorithm- and mission-dependent,  
 847 influenced by signal quality, onboard processing, antenna design, and orbit characteristics. The  
 848 findings highlight the crucial role of processing methodology in ensuring consistency and  
 849 accuracy in retrieving RO bending angle data, particularly when data from diverse missions  
 850 are used in operational weather forecasting systems. Future efforts in GNSS RO should focus  
 851 on developing harmonized processing standards and conducting inter-comparison studies to  
 852 quantify and mitigate structural uncertainty in bending angle datasets.

853  
 854 **5. Discussions and Summary**  
 855

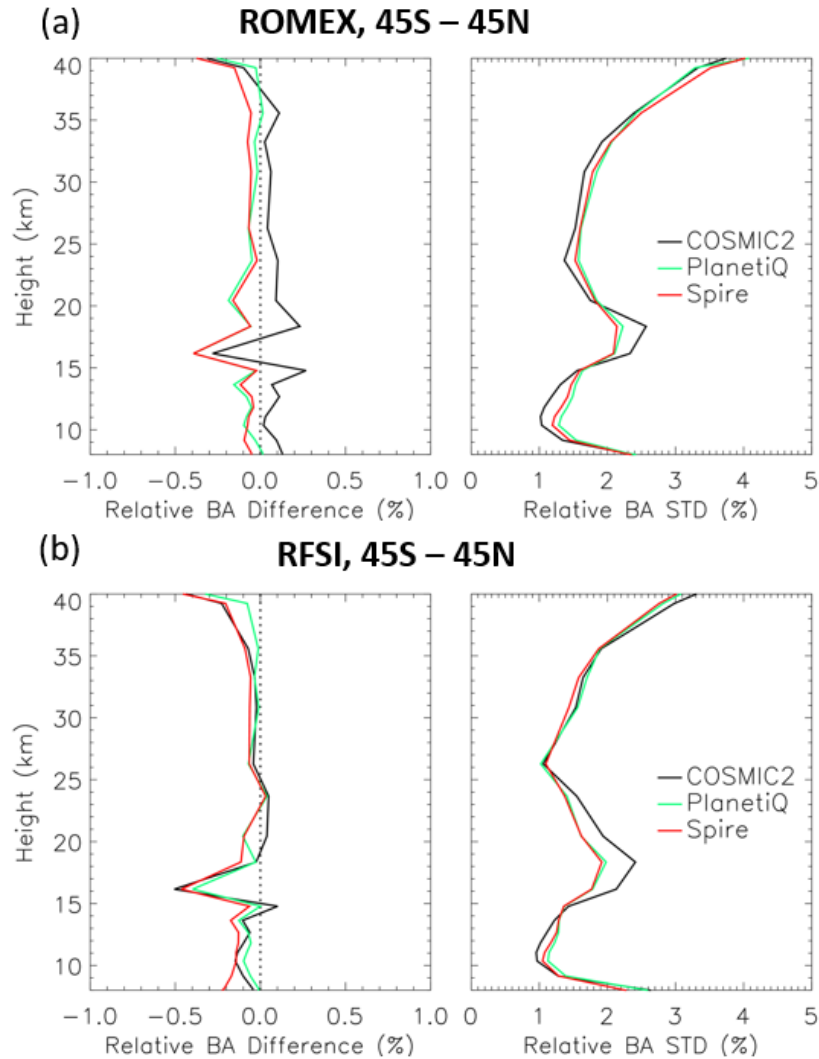
856 This study presents the first comprehensive cross-mission intercomparison of the STAR-  
 857 developed Full Spectrum Inversion algorithm with the community-standard ROPP CT2 and  
 858 EUMETSAT dataset within the framework of ROMEX. Using bending angle and refractivity  
 859 profiles from key GNSS RO missions (e.g., COSMIC-2, Spire, PlanetiQ, Metop-B/C) during  
 860 the ROMEX period (September–November 2022), we assessed inter-algorithm consistency  
 861 against ERA5 reanalysis and structural uncertainty against the three-dataset mean.

862  
 863 A significant finding is the excellent agreement among all three processing methods in the  
 864 middle and upper troposphere and lower stratosphere (8–35 km). In this region, the mean  
 865 bending angle differences remained within  $\pm 0.2\%$  and the standard deviations were below 3%,  
 866 demonstrating the maturity and robust internal coherence of RO observations across diverse

867 missions. Similarly, refractivity retrievals in this core region exhibited high stability, with mean  
868 biases within  $\pm 0.15\%$  and standard deviations typically below 1%.

869  
870 Anthes et al. (2025) reported that the UCAR-processed COSMIC-2 bending angles included  
871 in ROMEX exhibit a positive bias of approximately  $+0.1\text{--}0.15\%$  relative to ERA5 in the lower  
872 stratosphere, larger than the biases seen for Spire and other ROMEX datasets. Similar lower-  
873 stratospheric positive biases for UCAR COSMIC-2 have also been documented by Ho et al.  
874 (2024, 2025). This difference is predominantly a representativeness effect associated with  
875 orbit-dependent sampling over a non-spherical Earth (the azimuth effect), rather than a true  
876 systematic bias, and therefore does not significantly impact data assimilation. The remaining  
877 small component (less than 0.05%) is attributed to the sideways displacement of the occultation  
878 plane and can be mitigated by impact height correction during RO processing (Anthes et al.,  
879 2025). Figure 16 provides a zoomed-in comparison of the height-dependent fractional O–B  
880 bending-angle differences for the COSMIC-2, Spire, and PlanetiQ missions, between the  
881 EUMETSAT/UCAR processing and the STAR RFSI processing. In Fig. 16a, the COSMIC-2  
882 data are from UCAR, while the Spire and PlanetiQ datasets are processed by EUMETSAT; in  
883 Fig. 16b, all three missions are processed consistently by STAR RFSI.

884  
885 While the UCAR-provided COSMIC-2 ROMEX datasets show a small positive O–B bias  
886 compared to EUMETSAT-processed Spire and PlanetiQ data in the lower stratosphere (Fig.  
887 16a), the STAR RFSI-processed COSMIC-2 bending angles exhibit improved consistency with  
888 the Spire and PlanetiQ results (Fig. 16b). One contributing factor may be the treatment of  
889 horizontal tangent-point sliding within the RFSI framework. While a consistent occultation  
890 point definition is applied across missions in this study, differences in occultation point  
891 definitions (or georeferencing) among processing centers can affect the magnitude of the  
892 sliding-related correction. As noted in Anthes et al. (2025), UCAR defines the occultation point  
893 as the location where the L1 excess phase exceeds 500 m, typically in the lower troposphere.  
894 In contrast, ROPP defines it as the location where the straight-line tangent altitude equals zero,  
895 typically in the upper troposphere–lower stratosphere (UTLS). This sideways sliding effect can  
896 introduce a positive bias in COSMIC-2 bending angles of up to  $\sim 0.05\%$ . The underlying cause  
897 of the subtle differences in the lower-stratospheric O–B bending-angle among the processing  
898 centers (STAR, EUMETSAT, UCAR) will be ~~further~~ further examined further in future work.



899  
900  
901  
902  
903  
904

Fig. 16. Zoomed-in height-dependent fractional bending-angle differences (O–B) between RO observations and ERA5 simulations are shown for COSMIC-2, Spire, and PlanetiQ. Panels (a) and (b) display the mean bending-angle biases (left) and standard deviations (right) for RO data processed by EUMETSAT and by STAR RFSI, respectively.

905  
906  
907  
908  
909  
910  
911  
912  
913  
914  
915  
916  
917  
918

Conversely, larger discrepancies and heightened variability emerged in the lower troposphere (below ~8 km) and upper atmosphere (above ~35 km). These regions are challenged by multipath effects, increased tracking noise, and varying SNR. The FSI method, designed to resolve fine-scale atmospheric structures by leveraging full-spectrum signal information, demonstrated improved sensitivity in the lower atmosphere (Adhikari et al., 2021), particularly for missions such as PlanetiQ and Metop-B/C. However, it also showed increased variability and greater dependence on SNR cut-off and quality control thresholds, as seen with Spire and TerraSAR-X near the surface. In contrast, the CT2 method, while generally yielding smoother profiles with reduced noise, sometimes showed larger near-surface biases (e.g., CT2 for COSMIC-2 and Spire), suggesting a more conservative approach that might underestimate bending in complex conditions. EUMETSAT's dataset, in particular, achieved the smallest near-surface bending angle and refractivity biases across missions, indicating effective mitigation of noise and multipath.

919  
920

A crucial finding of this study is that structural uncertainty depends on both the processing algorithm and the satellite mission. A greater inter-method spread was observed across all

921 missions below 8 km, likely due to their distinct approaches to handling multipath, noise, and  
922 signal truncation. This structural uncertainty complicates the consistent use of multi-mission  
923 RO data. For instance, COSMIC-2 data processed by ROPP CT2 showed higher near-surface  
924 variability than those processed by RFSI and EUMETSAT. In contrast, missions like Metop-  
925 B/C exhibited stronger consistency across all three methods, while PlanetiQ demonstrated the  
926 highest inter-method consistency throughout the profile. These mission-specific patterns,  
927 clearly illustrated in Figs. 11-15, underscore the critical need to characterize and account for  
928 algorithmic effects when assimilating multi-mission RO data into operational weather  
929 forecasting systems. The explicit comparison of the total O-B standard deviation (Figs. 5-7)  
930 with the structural uncertainty (Figs. 11-15) quantifies the contribution of retrieval algorithm  
931 differences to the total error budget, demonstrating that structural differences account for  
932 approximately one-fourth of the total O-B standard deviation over all the altitudes, providing  
933 a critical metric for interpreting ROMEX forecast impact studies and refining GNSS RO data  
934 assimilation systems.

935

936 The ROMEX results unequivocally highlight the importance of quantifying algorithm-related  
937 structural uncertainty for data assimilation applications. To ensure a consistent and optimal  
938 representation of RO data in numerical weather prediction systems, it may be necessary to  
939 harmonize retrieval strategies across different processing centers or to apply mission- and  
940 algorithm-specific bias corrections.

941

942 The successful integration of STAR's FSI algorithm into ROPP version 10.0 represents a  
943 significant advancement, providing users with a robust and flexible alternative to existing  
944 algorithms. This enhancement facilitates consistent RO data processing across both  
945 government-funded and commercial missions, offering customizable settings to meet specific  
946 scientific and operational requirements.

947

948 In summary, this study demonstrates the critical influence of algorithm choice, particularly in  
949 the lower troposphere; confirms strong consistency among processors in the mid-to-upper  
950 atmosphere; identifies distinct mission-dependent structural uncertainties; and recommends  
951 applying bias correction or ensemble strategies to improve data assimilation. The findings  
952 strongly support continued efforts to harmonize across agencies through collaborative  
953 initiatives, such as ROMEX. As the volume and diversity of GNSS RO data continue to  
954 expand, these insights underscore the paramount need for robust algorithm development,  
955 thorough uncertainty quantification, and coordinated processing strategies to fully leverage RO  
956 observations and advance weather forecasting and climate monitoring capabilities.

957

958 **Code/Data availability.** The ROMEX data processed by EUMETSAT are available free of  
959 charge through ROM SAF, subject to the ROMEX terms and conditions. Further information  
960 is available at <https://irowg.org/ro-modeling-experiment-romex/> (last access: 28 March 2026).  
961 The ROMEX data processed by NOAA/STAR are available from STAR under the ROMEX  
962 terms and conditions. ERA5 data are available from the ECMWF data catalogue at  
963 <https://www.ecmwf.int/en/forecasts/datasets/browse-reanalysis-datasets> (last access: 28  
964 March 2026).

965

966 **Author contribution.** YC developed the RO processing system and designed the research  
967 plan, supervised the study, and prepared the manuscript. XZ conducted the data processing and  
968 prepared the figures and analysis. XJ contributed to the preparation of the data analysis and  
969 figures. SH provided overall scientific guidance throughout the project. XS and TL led the

970 theoretical development and conducted testing to improve the results. All co-authors  
971 contributed to the interpretation of the results and to the writing and revision of the manuscript.

972  
973 **Competing interests.** The contact author has declared that none of the authors has any  
974 competing interests.

975  
976 **Disclaimer. Publisher’s note:** Copernicus Publications remains neutral with regard to  
977 jurisdictional claims made in the text, published maps, institutional affiliations, or any other  
978 geographical representation in this paper. While Copernicus Publications makes every effort  
979 to include appropriate place names, the final responsibility lies with the authors. Views  
980 expressed in the text are those of the authors and do not necessarily reflect the views of the  
981 publisher.

982  
983 **Special issue statement.** This article is part of the special issue “The Radio Occultation  
984 Modeling EXperiment (ROMEX): observational quality, processing, and numerical weather  
985 prediction (NWP) applications”. It is not associated with a conference.

## 986 **Acknowledgments**

987  
988  
989 This research received no external funding and was supported by the NOAA Center for  
990 Satellite Applications and Research (STAR). We thank the ROMEX coordination team and the  
991 ROM SAF for facilitating access to the processed datasets. This work was further supported  
992 by the NOAA/NESDIS/STAR Product Development Readiness and Applications (PDRA)  
993 fund and by NOAA grants NA19NES4320002 and NA24NESX432C0001 (Cooperative  
994 Institute for Satellite Earth System Studies-CISESS) at the University of Maryland/ESSIC. The  
995 authors also thank Dr. Loknath Adhikari for his contributions to the development of the FSI  
996 algorithm, Josep Aparicio and two anonymous reviewers for their constructive suggestions,  
997 which have helped improve the quality and clarity of this manuscript. The scientific results and  
998 conclusions, as well as any views or opinions expressed herein, are those of the author(s) and  
999 do not necessarily reflect those of NOAA or the Department of Commerce.

## 1000 **References**

1001 Adhikari, A., Xie, F., and Haase, J. S.: Application of the full spectrum inversion algorithm to  
1002 simulated airborne GPS radio occultation signals, *Atmos. Meas. Tech.*, 9, 5077–5086,  
1003 <https://doi.org/10.5194/amt-9-5077-2016>, 2016.

1004  
1005  
1006 Adhikari, A., Ho, S.-P., and Zhou, X.: Inverting COSMIC-2 phase data to bending angle and  
1007 refractivity using the Full Spectrum Inversion method, *Remote Sens.*, 13, 1793,  
1008 <https://doi.org/10.3390/rs13091793>, 2021.

1009  
1010 Anthes, R. A.: Exploring Earth’s atmosphere with radio occultation: Contributions to weather,  
1011 climate, and space weather, *Atmos. Meas. Tech.*, 4, 1077–1103, [https://doi.org/10.5194/amt-](https://doi.org/10.5194/amt-4-1077-2011)  
1012 [4-1077-2011](https://doi.org/10.5194/amt-4-1077-2011), 2011.

1013  
1014 Anthes, R. A., Bernhardt, P. A., Chen, Y., Cucurull, L., Dymond, K. F., Ector, D., Healy, S.  
1015 B., Ho, S.-P., Hunt, D. C., Kuo, Y.-H., and others: The COSMIC/FORMOSAT-3 Mission:  
1016 Early Results, *Bull. Amer. Meteor. Soc.*, 89, 313–334, [https://doi.org/10.1175/BAMS-89-3-](https://doi.org/10.1175/BAMS-89-3-313)  
1017 [313](https://doi.org/10.1175/BAMS-89-3-313), 2008.

1019 Anthes, R. A., Marquardt, C., Ruston, B., and Shao, H.: Radio Occultation Modeling  
1020 Experiment (ROMEX): Determining the impact of radio occultation observations on numerical  
1021 weather prediction, *Bull. Amer. Meteor. Soc.*, 105, E1552–E1568,  
1022 <https://doi.org/10.1175/BAMS-D-23-0326.1>, 2024.

1023  
1024 Anthes, R., Sjoberg, J., Starr, J., and Zeng, Z.: Evaluation of biases and uncertainties in  
1025 ROMEX radio occultation observations, *Atmos. Meas. Tech.*, 18, 6997–7019, [EGUsphere](https://doi.org/10.5194/egusphereamt-18-6997-2025)  
1026 [\[preprint\]](https://doi.org/10.5194/egusphereamt-18-6997-2025), <https://doi.org/10.5194/egusphereamt-18-6997-2025>, 2025.

1027  
1028 Born, M. and Wolf, E.: *Principles of Optics*, Cambridge University Press, New York, 1999.

1029  
1030 Chen, Y., Zhou, X., Ho, S.-P., Shao, X., and Liu, T.-C.: Comparison of Radio Occultation  
1031 Bending Angle and Refractivity Processed by Different Inversion Algorithms from Multi-RO  
1032 Missions, in: *IGARSS 2024 IEEE Int. Geosci. Remote Sens. Symp.*, Athens, Greece, 2024,  
1033 8904–8907, <https://doi.org/10.1109/IGARSS53475.2024.10641034>, 2024.

1034  
1035 Cucurull, L., Derber, J. C., Treadon, R., and Purser, R. J.: Assimilation of global positioning  
1036 system radio occultation observations into NCEP’s Global Data Assimilation System, *Mon.*  
1037 *Weather Rev.*, 135, 3174–3193, <https://doi.org/10.1175/MWR3461.1>, 2007.

1038  
1039 Fjeldbo, G. F., Kliore, A. J., and Eshelman, V. R.: The neutral atmosphere of Venus as studied  
1040 with the Mariner V radio occultation experiments, *J. Astro.*, 76, 123–140, 1971.

1041  
1042 [Gorbunov, M., Irisov, V., and Rocken, C.: The Influence of the Signal-to-Noise Ratio upon](https://doi.org/10.3390/rs14122742)  
1043 [Radio Occultation Retrievals, \*Remote Sens.\*, 14, 2742, <https://doi.org/10.3390/rs14122742>,](https://doi.org/10.3390/rs14122742)  
1044 [2022a.](https://doi.org/10.3390/rs14122742)

1045  
1046 [Gorbunov, M., Irisov, V., and Rocken, C.: Noise Floor and Signal-to-Noise Ratio of Radio](https://doi.org/10.3390/rs14030691)  
1047 [Occultation Observations: A Cross-Mission Statistical Comparison, \*Remote Sens.\*, 14,](https://doi.org/10.3390/rs14030691)  
1048 [691, <https://doi.org/10.3390/rs14030691>, 2022b.](https://doi.org/10.3390/rs14030691)

1049  
1050 Gorbunov, M. E.: Radioholographic analysis of radio occultation data in multipath zones,  
1051 *Radio Sci.*, 37, 1008, <https://doi.org/10.1029/2000RS002577>, 2002a.

1052  
1053 Gorbunov, M. E.: Canonical transform method for processing radio occultation data in the  
1054 lower troposphere, *Radio Sci.*, 37, 1076, <https://doi.org/10.1029/2000RS002592>, 2002b.

1055  
1056 Gorbunov, M. E.: Ionospheric correction and statistical optimization of radio occultation data,  
1057 *Radio Sci.*, 37, <https://doi.org/10.1029/2000RS002370>, 2002c.

1058  
1059 Gorbunov, M. E., Lauritsen, K. B., Rhodin, A., Tomassini, M., and Kornblueh, L.: Analysis of  
1060 the CHAMP experimental data on radio-occultation sounding of the Earth’s atmosphere, *Izv.*  
1061 *Atmos. Ocean. Phys.*, 41, 798–813, 2005.

1062  
1063 Hajj, G. A., Kursinski, E. R., Romans, L. J., Bertiger, W. I., and Leroy, S. S.: A technical  
1064 description of atmospheric sounding by GPS occultation, *J. Atmos. Sol.-Terr. Phys.*, 64, 451–  
1065 469, [https://doi.org/10.1016/S1364-6826\(01\)00114-6](https://doi.org/10.1016/S1364-6826(01)00114-6), 2002.

1066  
1067 Healy, S. B.: Forecast impact experiment with a constellation of GPS radio occultation  
1068 receivers, *Atmos. Sci. Lett.*, 9, 111–118, <https://doi.org/10.1002/asl.169>, 2008.

1069  
1070 Hersbach, H., Bell, B., Berrisford, P., Biavati, G., Horányi, A., Muñoz Sabater, J., Nicolas, J.,  
1071 Peubey, C., Radu, R., Rozum, I., Schepers, D., Simmons, A., Soci, C., Dee, D., and Thépaut,  
1072 J.-N.: ERA5 hourly data on pressure levels from 1940 to present, Copernicus Climate Change  
1073 Service (C3S) Climate Data Store (CDS) [data set], <https://doi.org/10.24381/cds.bd0915c6>,  
1074 accessed: 6 August 2024.  
1075  
1076 [Hedin, A. E., Extension of the MSIS thermosphere model into the middle and lower](#)  
1077 [atmosphere, \*J. Geophys. Res.\*, 96, 1159–1172, 1991.](#)  
1078  
1079 Ho, S.-P., Anthes, R. A., Ao, C. O., Healy, S., Horányi, A., Hunt, D., Mannucci, A. J.,  
1080 Pedatella, N., Randel, W. J., and Simmons, A.: The COSMIC/FORMOSAT-3 Radio  
1081 Occultation Mission after 12 Years: Accomplishments, Remaining Challenges, and Potential  
1082 Impacts of COSMIC-2, *Bull. Amer. Meteor. Soc.*, 101, E1107–E1136,  
1083 <https://doi.org/10.1175/BAMS-D-19-0027.1>, 2020.  
1084  
1085 Ho, S.-P., Hunt, D., Steiner, A. K., Mannucci, A. J., Kirchengast, G., Gleisner, H., Heise, S.,  
1086 von Engeln, A., Marquardt, C., Sokolovskiy, S., Schreiner, W., Scherllin-Pirscher, B., Ao, C.,  
1087 Wickert, J., Syndergaard, S., Lauritsen, K. B., Leroy, S., Kursinski, E. R., Kuo, Y.-H.,  
1088 Foelsche, U., Schmidt, T., and Gorbunov, M.: Reproducibility of GPS radio occultation data  
1089 for climate monitoring: Profile-to-profile inter-comparison of CHAMP climate records 2002  
1090 to 2008 from six data centers, *J. Geophys. Res.*, 117, D18111,  
1091 <https://doi.org/10.1029/2012JD017665>, 2012.  
1092  
1093 Ho, S.-P., Zhou, X., Shao, X., Chen, Y., Jing, X., and Miller, W.: Using the Commercial GNSS  
1094 RO Spire Data in the Neutral Atmosphere for Climate and Weather Prediction Studies, *Remote*  
1095 *Sens.*, 15, 4836, <https://doi.org/10.3390/rs15194836>, 2023.  
1096  
1097 Ho, S.-P., Shao, X., Chen, Y., Zhou, J., Gu, G., Miller, W., and Jing, X.: Lessons Learned from  
1098 the Preparation and Evaluation of Multiple GNSS RO Data for the ROMEX from  
1099 NOAA/STAR. Presentation at the COSMIC/JCSDA Workshop and IROWG-10, Boulder,  
1100 Colorado, 12-18 September 2024. Available at: [https://www.cosmic.ucar.edu/events/cosmic-](https://www.cosmic.ucar.edu/events/cosmic-jcsda-workshop-irowg-10/agenda)  
1101 [jcsda-workshop-irowg-10/agenda](https://www.cosmic.ucar.edu/events/cosmic-jcsda-workshop-irowg-10/agenda), 2024.  
1102  
1103 Ho, S.-P., Shao, X., Chen, Y., Zhou, J., and Miller, W.: Advances in ROMEX data processing  
1104 and evaluation: Lessons from NOAA STAR. Presentation at the 2nd ROMEX Workshop,  
1105 February 27, 2025, at EUMETSAT, Darmstadt, Germany. Available at  
1106 <https://www.eventsforce.net/romex2025>, 2025.  
1107  
1108 Jensen, A. S., Lohmann, M., Benzon, H.-H., and Nielsen, A. S.: Full spectrum inversion of  
1109 radio occultation signals, *Radio Sci.*, 38, 1040, <https://doi.org/10.1029/2002RS002763>, 2003.  
1110  
1111 Jensen, A. S., Lohmann, M., Nielsen, A. S., and Benzon, H.-H.: Geometrical optics phase  
1112 matching of radio occultation signals, *Radio Sci.*, 39, RS3009,  
1113 <https://doi.org/10.1029/2003RS002899>, 2004.  
1114  
1115 Kursinski, E. R., Hajj, G. A., Schofield, J. T., Linfield, R. P., and Hardy, K. R.: Observing  
1116 Earth’s atmosphere with radio occultation measurements using the Global Positioning System,  
1117 *J. Geophys. Res.*, 102, 23429–23465, <https://doi.org/10.1029/97JD01569>, 1997.  
1118

1119 Luzum, B. and Petit, G.: The IERS conventions (2010): Reference systems and new models,  
1120 Proc. Int. Astron. Union, 10, 227–228, 2012.  
1121

1122 Miller, W., Chen, Y., Ho, S.-P., and Shao, X.: Exploring the Value of Spire GNSS Radio  
1123 Occultation Bending Angle Assimilation for Improving HWRP Model Forecasts of Atlantic  
1124 Hurricane Intensity, Weather and Forecasting, 40 (6), 809-827, [https://doi.org/10.1175/waf-d-](https://doi.org/10.1175/waf-d-24-0092.1)  
1125 [24-0092.1](https://doi.org/10.1175/waf-d-24-0092.1), 2025.  
1126

1127 [Paolella, S., et al. \(2025\). Assessment of operational non-time-critical Sentinel-6A Michael](#)  
1128 [Freilich radio occultation data: insights into tropospheric GNSS signal cut-off strategies and](#)  
1129 [processor improvements. Atmos. Meas. Tech., 18, 2825–2845. \[https://doi.org/10.5194/amt-18-\]\(https://doi.org/10.5194/amt-18-2825-2025\)](#)  
1130 [2825-2025](https://doi.org/10.5194/amt-18-2825-2025)

1131

1132 Petit, G. and Luzum, B. (Eds.): IERS Technical Note No. 36, IERS, Frankfurt am Main, 2010,  
1133 available at: <https://apps.dtic.mil/sti/citations/ADA535671> (last access: 6 August 2024).  
1134

1135 Rocken, C., Anthes, R., Exner, M., Hunt, D., Sokolovskiy, S., Ware, R., Gorbunov, M.,  
1136 Schreiner, W., Feng, D., Herman, B., Kuo, Y.-H., and Zou, X.: Analysis and validation of  
1137 GPS/MET data in the neutral atmosphere, J. Geophys. Res.-Atmos., 102, 29849–29866,  
1138 <https://doi.org/10.1029/97JD02400>, 1997.  
1139

1140 Schreiner, W. S., Weiss, J. P., Anthes, R. A., Braun, J., Chu, V., Fong, J., Hunt, D., Kuo, Y.-  
1141 H., Meehan, T., Serafino, W., Sjoberg, J., Sokolovskiy, S., Talaat, E., Wee, T. K., and Zeng,  
1142 Z.: COSMIC-2 radio occultation constellation: First results, Geophys. Res. Lett., 47,  
1143 [e2019GL086841](https://doi.org/10.1029/2019GL086841), <https://doi.org/10.1029/2019GL086841>, 2020.  
1144

1145 Shao, H., and Folsche, U.: ROMEX: Status and First Lessons Learned, Presentation at IROWG  
1146 CGMS-52 Plenary, 2024, Washington, DC, USA. Available at [https://irowg.org/wpcms/wp-](https://irowg.org/wpcms/wp-content/uploads/2025/04/CGMS-52-IROWG-WP-03.pdf)  
1147 [content/uploads/2025/04/CGMS-52-IROWG-WP-03.pdf](https://irowg.org/wpcms/wp-content/uploads/2025/04/CGMS-52-IROWG-WP-03.pdf), 2024.  
1148

1149 [Sokolovskiy, S., Rocken, C., Schreiner, W., Hunt, D., and Johnson, J.: Postprocessing of L1](#)  
1150 [GPS radio occultation signals recorded in open-loop mode, Radio Sci., 44, RS2002,](#)  
1151 <https://doi.org/10.1029/2008RS003907>, 2009.  
1152

1153 Sokolovskiy, S., Rocken, C., Schreiner, W., and Hunt, D.: On the uncertainty of radio  
1154 occultation inversions in the lower troposphere, J. Geophys. Res., 115, D22111,  
1155 <https://doi.org/10.1029/2010JD014058>, 2010.  
1156

1157 Steiner, A. K., Lackner, B. C., Pirscher, B., Hegerl, G. C., and Foelsche, U.: The contribution  
1158 of radio occultation to the assessment of tropospheric temperature trends, J. Climate, 24, 4936–  
1159 4950, <https://doi.org/10.1175/2011JCLI3982.1>, 2011.  
1160

1161 Steiner, A. K., Ladstädter, F., Ao, C. O., Gleisner, H., Ho, S.-P., Hunt, D., Schmidt, T.,  
1162 Foelsche, U., Kirchengast, G., Kuo, Y.-H., and others: Consistency and structural uncertainty  
1163 of multi-mission GPS radio occultation records, Atmos. Meas. Tech., 13, 2547–2575,  
1164 <https://doi.org/10.5194/amt-13-2547-2020>, 2020.  
1165

1166 The Radio Occultation Processing Package (ROPP) Pre-processor Module User Guide, version  
1167 10.0, ROM SAF Consortium, Ref: SAF/ROM/METO/UG/ROPP/004, 30 September 2020.  
1168

1169 Vorob'ev, V. V. and Krasil'nikova, T. G., Estimation of the accuracy of the atmospheric  
1170 refractive index recovery from Doppler shift measurements at frequencies used in the  
1171 NAVSTAR system, *USSR Phys. Atmos. Ocean, Engl. Transl.*, 29, 602–609, 1994.